Graphical Abstract

Frequency-Dependent Neurostimulation in Whole Brain Network models

Mónica Otero, Elida Poo, Felipe Torres, Cristobal Mendoza, Caroline Lea-Carnall, Alejandro Weinstein, Pamela Guevara, Pavel Prado, Joana Cabral, Wael El-Deredy

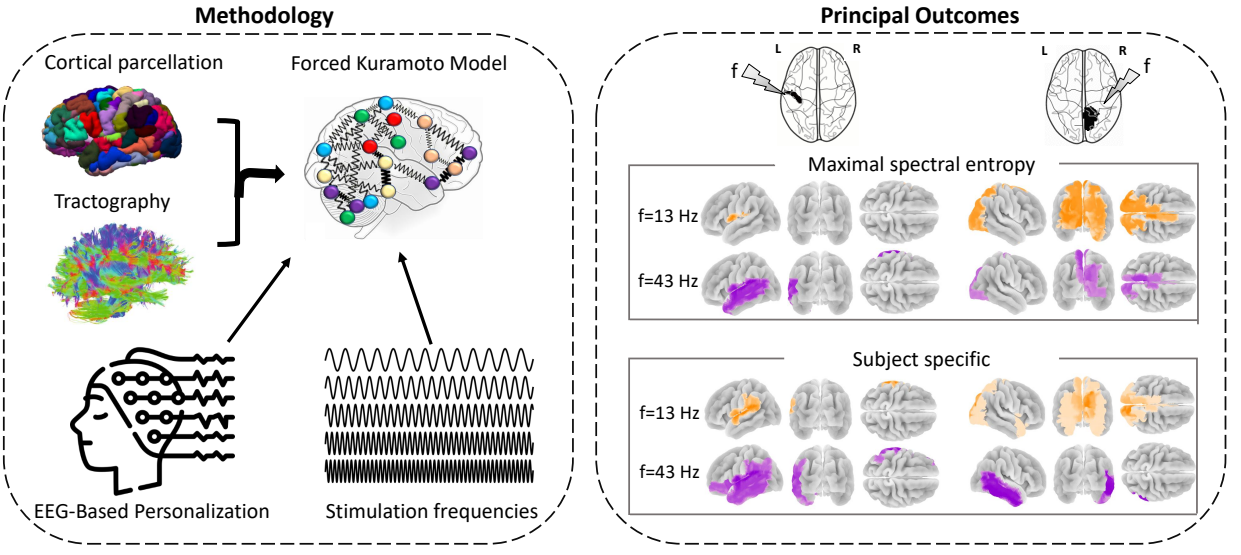

Highlights

Frequency-Dependent Neurostimulation in Whole Brain Network models

Mónica Otero, Elida Poo, Felipe Torres, Cristobal Mendoza, Caroline Lea-Carnall, Alejandro Weinstein, Pamela Guevara, Pavel Prado, Joana Cabral, Wael El-Deredy

- A forced Kuramoto model captures frequency-dependent brain network entrainment.
- Stimulation entrains specific brain regions based on frequency and target site.
- Entrainment spreads beyond direct connections, influencing distant brain regions.
- Changes in model parameters shape activation patterns and frequency tuning.
- Model is validated by sensory stimulation producing EEG-like activation patterns.

Frequency-Dependent Neurostimulation in Whole Brain Network models

Mónica Otero[a,b], Elida Poo[c], Felipe Torres[d], Cristobal Mendoza[c], Caroline Lea-Carnall[f,g], Alejandro Weinstein[h], Pamela Guevara[c], Pavel Prado[e], Joana Cabral[i] and Wael El-Deredy[k,*]

[a] *Facultad de Ingeniería,Universidad San Sebastián, Santiago de Chile, Chile*
[b] *Fundación Ciencia y Vida, Santiago de Chile, Chile*
[c] *Department of Electrical Engineering, Faculty of Engineering, Universidad de Concepción, Concepción, Chile*
[d] *Departamento de Computación e Industrias, Facultad de Ciencias de la Ingeniería, Universidad Católica del Maule, , Talca, Chile*
[f] *School of Health Sciences, Faculty of Biology, Medicine and Health, University of Manchester, Manchester, United Kingdom*
[g] *Manchester Academic Health Science Center, University of Manchester, Manchester, United Kingdom*
[h] *Department of Electronic Engineering, Universidad Técnica Federico Santa María, Valparaíso, Chile*
[e] *Escuela de Fonoaudiología, Universidad San Sebastián , Santiago de Chile, Chile*
[i] *Life and Health Sciences Research Institute, Minho University, Braga, Portugal*
[k] *Brain Dynamics Lab, Interdisciplinary Center of Biomedical and Engineering Research for Health, Universidad de Valparaíso, Valparaíso, Chile*

ARTICLE INFO

Keywords:
neurostimulation
frequency-dependent entrainment
forced Kuramoto model
neural entrainment

Abstract

Background

Neuromodulation with electric, electromagnetic, or sensory stimulation presents a complex challenge in optimizing stimulation parameters to achieve specific physiological, cognitive, or behavioral outcomes. The effectiveness of stimulation depends on factors such as stimulation frequency, target location, and individual brain network architecture, yet a systematic framework for predicting stimulation effects is still lacking.

Methods

We deployed a coupled oscillators Kuramoto model informed by the human structural connectome, known to generate spontaneous metastable oscillatory modes with dynamical features resembling real M/EEG oscillatory activity. We simulated the effect of the stimulation at the peaks of its oscillatory modes in different brain cortical regions, using different structural connectivity properties to emulate inter-individual variability. We investigated how periodic stimulation influences network oscillatory activity and functional dynamics by identifying brain regions that synchronize with the stimulation frequency.

Results

Neurostimulation outcomes are functionally selective, and vary depending on both the stimulation frequency and the structural connectivity of the stimulated region. Nodes with the greatest sum of adjacent connection weights facilitated broader network engagement, while variability in structural connectivity led to specific entrainment patterns. Entrainment exhibited an inverse relationship with frequency, such that lower-frequency stimulation propagated more extensively across the network, while higher-frequency inputs produced more spatially confined effects.

Conclusions

Our computational modeling aligns with empirical findings on oscillatory communication, demonstrating that network-based approaches can enhance neurostimulation selectivity by incorporating individual structural connectivity and the frequency-dependent nature of entrainment. These results support a model-driven framework for personalized, context-specific stimulation, advancing the precision and predictability of neuromodulation strategies.

1. Introduction

In recent years, increasing evidence has emerged describing how non-invasive periodic stimulation techniques, such as transcranial alternating current stimulation (tACS), repetitive transcranial magnetic stimulation (rTMS), theta

*Wael El-Deredy
wael.el-deredy@uv.cl (W. El-Deredy)
ORCID(s): 0000-0002-9822-1092 (W. El-Deredy)

burst stimulation (TBS), and repetitive sensory stimulation (e.g. visual, auditory or tactile), can be used to modulate oscillatory brain activity [39, 47, 74, 84, 85]. These methods aim to entrain neural networks by stimulating brain regions, thereby enhancing cognitive processes and restoring or reconfiguring dysfunctional neural activity associated with neurological and psychiatric disorders [4, 7, 96]. For instance, rTMS at gamma frequencies (30-80 Hz) has shown potential in reducing symptoms of schizophrenia [7], while tACS targeting alpha oscillations (8-12 Hz) has been used to alleviate symptoms in major depressive disorder [4]. Furthermore, sensory stimulation, such as rhythmic auditory stimulation, has been shown to improve motor function in Parkinson's disease by entraining beta oscillations (13-30 Hz) [96].

However, the outcomes of such neuromodulation techniques are variable, as the underlying mechanisms that govern entrainment and signal propagation within large-scale brain networks are not fully understood, therefore impacting their efficacy. Gaining deeper insight into how stimulation parameters, such as frequency and stimulation site, interact with complex oscillatory brain dynamics is crucial to optimizing possible therapeutic interventions. An effective strategy to address this challenge is the use of computational models, which enables the systematic exploration and refinement of the theoretical range of stimulation parameters essential to achieve effective neurostimulation [55].

Oscillations in neural systems are observed across multiple spatial and temporal scales, from individual neurons to whole-brain networks. Neural oscillations are thought to play a crucial role in coordinating neural activity, allowing the brain to integrate information across different regions and timescales [12]. This integration supports essential cognitive processes such as perception, attention, and memory [8, 36, 53]. At the local circuit level, oscillatory activity is commonly observed in local field potentials (LFP), with representative frequencies around 40 Hz [13, 35]. Oscillatory activity at the macroscopic level is generally slower and strongly influenced by network interactions [79], contributing to complex brain dynamics [15, 58]. The interplay between local intrinsic dynamics and global connectivity structures results in a metastable system, where brain networks exhibit transient synchronization patterns that can rapidly switch between different states [11, 15, 90], supporting the brain's ability to adapt to changing cognitive demands and environmental conditions [43, 76].

Computational models of whole-brain dynamics provide a powerful framework for understanding how stimulation interacts with the brain's oscillatory dynamics. Large-scale network models simulate the interplay between local oscillatory activity and large-scale connectivity, providing a controlled environment to investigate mechanisms of neural entrainment. The choice of model for the network nodes depends on the specific research question, for example Kuramoto oscillators describe phase synchronisation [54], Stuart-Landau oscillators allow for the inclusion of amplitude [57], or the more biologically realistic Wilson-Cowan model describes a pair of interacting populations of nodes (excitatory and inhibitory) [94]. Recent work has highlighted how network structure, such as conduction delays and network topology, critically shapes emergent spectral properties of brain activity, influencing the way oscillations propagate through the brain [15, 20, 90]. For instance, Torres et al. (2024) demonstrated that multiple coherent subnetworks can emerge spontaneously from a single connectome-based oscillator model, while Castro et al. (2020) showed that cortical ignition dynamics are tightly linked to the core organization of the human connectome. In addition, network size and connectivity constraints have been found to determine the dominant cortical frequencies [59], highlighting the role of anatomical architecture in shaping global oscillatory dynamics.

Integrating computational modeling with neuroimaging technologies holds great promise for improving the precision and efficacy of brain stimulation. Despite recent advances, the challenge remains to identify optimal stimulation parameters tailored to individual neurophysiological profiles. Whole-brain models incorporating realistic structural and functional connectivity data offer a promising approach to guide personalized neuromodulation interventions. In this study, we systematically investigated how periodic stimulation influences neural entrainment and its propagation in a whole-brain network model. We varied stimulation site and frequency, network coupling strength, and neural delays to assess how entrainment depends on local node properties, whether it propagates beyond directly stimulated regions, and to what extent frequency-specific focal stimulation can modulate the activity of deeper brain structures. Furthermore, we investigated how entrainment depends on the baseline network dynamics and whether stimulation of sensory areas at specific frequencies aligns with experimentally observed EEG patterns.

2. Materials and Methods

This section describes the methodology of our study, in which we implemented a Forced Kuramoto model to simulate brain dynamics under external stimulation using a network topology derived from human Diffusion Tensor

Imaging (DTI) data. To achieve this, we modified the classic Kuramoto model [54] by incorporating time delays [16] and introducing an external periodic force [68] applied to individual nodes.

This approach allows us to explore how stimulation influences entrainment patterns in brain networks. Specifically, we examine the impact of stimulation site and stimulation frequency, as well as the role of intrinsic parameters of the model, such as mean time delays and coupling strengths between brain regions.

We initially identified the model parameters that maximized model metastability (determined to be the point of maximal spectral entropy, as in [90]) by exploring the parameter space defined by global coupling strength and fixed these for all remaining experiments. We tested the effect of stimulation frequency and site by systematically stimulating each node individually and identifying which nodes of the network were entrained.

2.1. Brain network model with Kuramoto oscillators

To explore the spontaneous dynamics of coupled brain areas, we used a variation of the classic Kuramoto model [54] incorporating time delays between connected brain regions to enhance neurobiological realism [16, 17]. The dynamical equation that describes the behavior of the phase $\theta_n(t)$ of a node n at time t, is represented by:

$$\dot{\theta}_n(t) = \omega_n + K \sum_{p=1}^{N} c_{np} \sin(\theta_p(t - \tau_{np}) - \theta_n(t)), \tag{1}$$

where ω_n is the natural frequency of the oscillator n, assumed to be identical across all oscillators, and set to $\omega_n = 2\pi 40$ Hz. The use of 40 Hz as the intrinsic frequency for local oscillators in the whole-brain models is a modeling convention grounded in experimental neuroscience. It reflects the presence of gamma-band activity commonly observed in cortical dynamics and provides a biologically plausible regime for investigating neural synchronization, oscillatory propagation, and emergent large-scale network behavior. Deco et al. (2009) and subsequent computational studies [15, 17, 90] have maintained this assumption to simplify model design while effectively capturing the essential features of gamma-band neural synchrony. Additionally, using 40 Hz facilitates comparability across modeling studies and alignment with empirical EEG and MEG data.

In Equation 1 the parameter K represents the global coupling strength between oscillators. The network structure is represented by two N-by-N matrices: the connection weight matrix (C), where each element is proportional to the number of detected white matter tracts between two regions, and the inter-regional delay matrix (D), which accounts for transmission latencies between brain regions. The elements c_{np} and d_{np} represent the connection weight and delay, respectively, between two brain regions n and p and N is the number of nodes. To better understand the role of delays in the system, a mean delay factor (MD) is introduced, corresponding to the mean of the delay distribution. Since the distances between nodes remain fixed, varying MD is equivalent to modifying the conduction velocity (v) of neuronal signals [17], allowing the delays to be expressed as:

$$\tau_{np} = \mathrm{MD} \cdot d_{np}. \tag{2}$$

In this study, we used the structural brain network from Cabral et al. (2014), constructed using the AAL90 parcellation template [91], which segments the brain into 90 regions that define the network oscillators or nodes. Connectivity was derived using probabilistic tractography, which estimates white matter tracts between brain regions [9] using DTI data of 21 healthy participants [17]. This connectome was initially used by Cabral et al. (2014) to model delayed interactions leading to frequency-specific amplitude modulations that resemble MEG resting-state networks. More recently, Torres et al. (2024) employed the same anatomical framework to study metastable dynamics and the spontaneous emergence of coherent subnetworks at distinct frequencies.

To characterize the system's dynamics, we quantify metastability using spectral entropy, which reflects the energy distribution across frequencies and indicates the system's adaptability to stimulation. A more peaked spectrum corresponds to lower spectral entropy, signifying higher synchronization, while a flatter spectrum indicates greater variability and reduced synchronization [48]. This pattern has been observed in EEG studies, where deep sleep or seizures show low entropy, whereas wakeful states exhibit higher entropy [42, 45, 90]. Spectral entropy (SE) is calculated using Shannon's entropy formula, where power values are normalized and treated as probabilities, as shown

in the following equation:

$$\mathrm{SE}_n = -\sum_{i=1}^{N} P(f_i) \log P(f_i), \tag{3}$$

where $P(f_i))$ is the normalized power spectral density at frequency f_i. Additionally, the spectral entropy is summed across all nodes to provide a comprehensive measure of the overall system:

$$\mathrm{SE} = \sum_{n=1}^{N} \mathrm{SE}_n. \tag{4}$$

2.2. Modelling stimulation using Forced Kuramoto

Moreira and de Aguiar (2019) introduced a Forced Kuramoto model to examine the conditions required for global synchronization, considering the fraction of forced nodes and their dependence on network topology. Building on this framework, our model integrates an external periodic force that targets a single oscillator at a time while accounting for time delays in interactions. The governing equation is:

$$\dot{\theta}_n(t) = \omega_n + A\delta_{n,E} \sin(2\sigma t - \theta_n) + K \sum_{p=1}^{N} c_{np} \sin(\theta_p(t - \tau_{np}) - \theta_n(t)), \tag{5}$$

where A represents the amplitude of the external force and defines the coupling strength between the stimulus and the stimulated node. A fixed stimulation amplitude of $A = 400$ was used in all simulations, as this was the minimum amplitude at which the stimulated node optimally synchronized with the stimulus for all frequencies. The parameter $\sigma = 2\pi f$, where f denotes the stimulation frequency. E identifies the node subjected to the external force, with $\delta_{n,E} = 1$ if n is equal to E and zero otherwise.

Simulations were conducted under two possible conditions. The first, referred to as the baseline, is a network in which the system operates without the influence of any external force according to Eq. 1. The second condition, termed the stimulation state, introduces an external periodic force (Eq. 5).

Each simulation was run for 600 seconds, with external stimulation applied between 300 and 600 seconds. Stimulation was applied separately to each network node, and for each node, simulations were performed independently at each of the frequency values $f = 13.0, 15.0, 29.4, 41.2, 43.0$ Hz. These frequencies correspond to the dominant peaks identified at the point of maximum spectral entropy ($K = 4$, MD = 21 ms) during baseline. This point, highlighted by the yellow square in Figure 1, is part of the broader parameter space fully mapped in Figure S1, as reported by Torres et al. (2024). The lower panel of Figure 1 illustrates the spectral profile at this maximum entropy point.

In addition, we performed simulations with different values of K and MD to account for individual spectral differences. To explore this, we used the point of maximum entropy at baseline, as well as specific points matching the spectral features obtained from EEG recordings of young, healthy participants (see next section for details about how we set the values of K and MD).

2.3. EEG data processing and mapping to Kuramoto spectral space

To illustrate how sensitivity to stimulation depends on the baseline network properties, we used real EEG data from Otero et al.(2020). Specifically, we examined how baseline spectral characteristics influence the response to stimulation by fitting the model spectrum to those obtained from experimental EEG recordings in their study.

Eyes-open ongoing EEG recordings from Otero et al.(2020) were obtained from 19 healthy participants (11 males, 8 females; age = 26 ± 3 years) with normal or corrected-to-normal vision and no reported history of epilepsy, neurological, or psychiatric disorders. The study followed ethical guidelines and was approved by the Research and Ethics Committee of the Universidad de Valparaíso (evaluation statement code CEC170-18). Written informed consent was obtained from all participants.

EEG recordings were acquired using a Biosemi Acquisition System from 64 scalp electrodes arranged in a radial configuration. The signals were sampled at 8 kHz and pre-processed offline using Brain Vision Analyzer 2.0. Pre-processing included re-referencing to the average of all channels, band-pass filtering between 0.1 and 200 Hz with an 8th-order zero-phase shift Butterworth filter, and downsampling to 512 Hz. To remove artifacts from eye blinks and

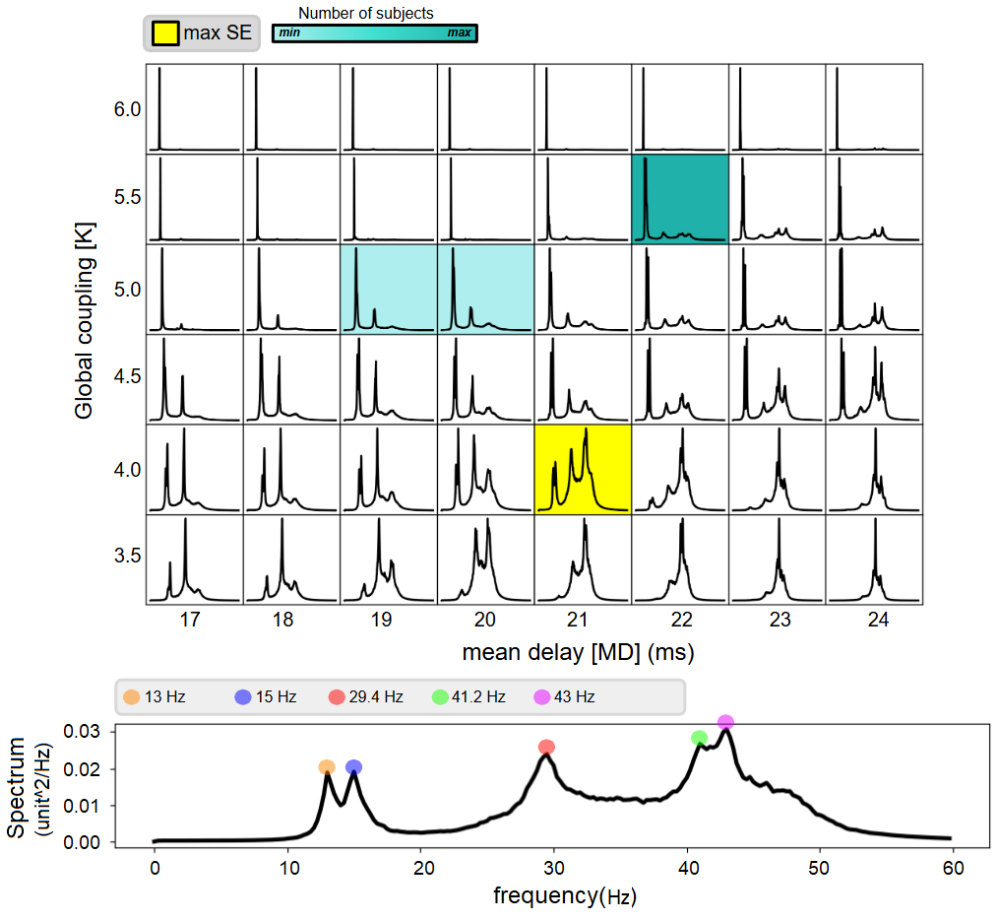

Figure 1: Multistate metastability in Kuramoto whole-brain network model. Top: Average spectra as a function of K and MD. The yellow square indicates the parameter set (global coupling K=4, mean delay MD=21 ms) corresponding to maximum spectral entropy. Cyan squares indicate the model's parameter space whose spectral entropy matched the spectral entropy of real EEG data: $\{K, \text{MD}\} = \{5, 19 \text{ ms}\}$; $\{5, 20 \text{ ms}\}$ and $\{5, 22 \text{ ms}\}$. Color intensity represents the number of participants whose EEG spectra aligned with each parameter set. Bottom: Average spectrum at maximum spectral entropy. The peaks agree with the spontaneous oscillatory modes that emerge from the model dynamics with parameter set to 4, 21ms, as reported by Torres et al. 2024, which in turn map onto specific frequency-dependent functional networks ([15, 17, 90]). We used these frequencies to stimulate the network using Equation 1.

movements, Independent Component Analysis (ICA) was applied. For further analysis, the cleaned EEG data were segmented into 5-second epochs.

To identify the model spectra that best matched the EEG spectra of the participants, we compared the mean EEG spectrum of each subject to the mean model spectra across a range of parameters (K and MD), following a methodology similar to that of a previous study conducted without stimulation [90].

The mean spectrum for each participant was obtained by averaging the power spectral density (PSD) across all electrode signals. Similarly, the mean model spectra for each parameter set were derived by averaging the PSD across all nodes in the network. The spectrum was calculated using Welch's method with a Hann window of 5 seconds and a 50% overlap, resulting in a frequency resolution of 0.2 Hz. To quantify the similarity between every participant and model spectra, we used the Jensen-Shannon distance (JSD), a symmetric and smoothed variant of the Kullback-Leibler (KL) divergence. This metric ranges from 0 (indicating identical distributions) to 1 (indicating maximal divergence) [61].

Mathematically, the Jensen-Shannon divergence between two probability distributions P and Q is given by:

$$\mathrm{JSD}(P\|Q) = \frac{1}{2}D_{\mathrm{KL}}(P\|Q) + \frac{1}{2}D_{\mathrm{KL}}(Q\|P), \tag{6}$$

where $M = \frac{1}{2}(P+Q)$ is the average distribution between P and Q, and $D_{\mathrm{KL}}(P\|Q)$ is the Kullback-Leibler divergence, defined as:

$$D_{\mathrm{KL}}(P\|Q) = \sum_i P(i)\log\frac{P(i)}{Q(i)}. \tag{7}$$

Using this approach, we identified parameter combinations that closely matched the model and participants' EEG spectra, which can be interpreted as individual fingerprints reflecting subject-specific oscillatory dynamics. The mapping of the model spectra to real EEG data is shown in Figure S2. The selected values were: $\{K, \mathrm{MD}\} = \{5, 19\ \mathrm{ms}\}$; $\{5, 20\ \mathrm{ms}\}$ and $\{5, 22\ \mathrm{ms}\}$ (cyan squares in Figure 1). The last combination also represents the average across all participants.

To better understand how these parameter combinations shape the network's baseline temporal dynamics, we analyzed the duration of metastable oscillatory modes (MOMs) across the selected K and MD values. MOMs duration indicates the stability of transient oscillatory states, revealing how long dominant frequency components persist before shifting to a new state [15, 90] (see Supplementary Section 8.2). As shown in Figure S3, for K and MD values yielding spectral properties consistent with EEG recordings, alpha-band oscillations emerged as the dominant component in both temporal persistence and spatial distribution. However, this dominance was not uniform across the full parameter space, highlighting the necessity of carefully selecting K and MD values to reproduce realistic oscillatory behavior.

2.4. Measuring entrainment and propagation in the Network

Neural entrainment was induced using sinusoidal stimulation, which mimics external rhythmic input to the system. The stimulation signal was defined as a sinusoidal oscillation of the form: $A\sin(2\pi f)$, applied systematically to each node at a specific frequency. This frequency was chosen to coincide with the peaks of the global averaged spectrum generated by the model with parameters set to match those at the point of maximum spectral entropy, as these represent the emergent oscillatory modes of the system. These frequency peaks are associated with limit-cycle attractors, meaning that neural activity at these frequencies tends to persist for extended periods, reflecting the multi-state metastable dynamics of the network [90].

Selecting these preferred frequencies ensures that stimulation aligns with the system's natural oscillatory states, optimizing the potential for entrainment and functional modulation. Furthermore, prior studies have demonstrated that the spectrum generated at maximal spectral entropy correlates well with brain states characterized by wakefulness and dynamic flexibility, whereas deviations from this point are associated with altered states such as sleep or anesthesia [90]. Thus, stimulating at these frequencies provides a biologically relevant way to probe network adaptability and propagation of entrainment.

A node is considered entrained if it meets two criteria:

1. Spectral Amplitude Criterion: The spectral amplitude at the stimulation frequency must exceed twice the baseline value. This ensures that the stimulation induces a significant and measurable response beyond the node's intrinsic activity.
2. Phase-Locking Criterion: The Phase-Locking Value (PLV) between the node and the stimulation signal must exceed 70%, indicating strong and consistent phase synchronization over time. PLV is computed as:

$$\mathrm{PLV} = \frac{1}{N}\sum_{n=1}^{N} e^{j(\theta_1(n)-\theta_2(n))}, \tag{8}$$

where N represents the number of time points, $\theta_1(n)$ and $\theta_2(n)$ are the instantaneous phases of the two signals at time point n, and $e^{j(\cdot)}$ denotes the complex exponential of the phase difference [5]. A PLV greater than 70% indicates a strong and consistent synchronization with the stimulation signal.

We define entrainment propagation as the phenomenon in which a node becomes entrained despite lacking a direct structural connection to the stimulated node. This indirect entrainment arises as stimulation effects spread through

intermediate nodes, influencing other network regions. The ability of the system to transmit and distribute stimulation effects underscores its potential to induce widespread dynamic changes in network activity.

To further investigate this phenomenon, we examined whether entrainment is influenced by the network's structural properties. Specifically, we evaluated the linear relation between the number of entrained nodes and various network metrics, including weighted degree, betweenness centrality, degree centrality, closeness centrality, and connection delays (see Supplementary Material Section 8.3). Among these, weighted degree exhibited the strongest correlation with entrainment, suggesting that nodes with a higher total connection weight are more likely to facilitate the propagation of entrainment throughout the network.

2.5. Simulations Design

We conducted a series of simulations to systematically examine how stimulation frequency, location, and baseline network state interact to shape neural entrainment and its propagation. To this end, we varied stimulation site, frequency, and network coupling and delay parameters to assess how entrainment depends on node properties, whether it propagates beyond directly stimulated regions, and the extent to which frequency focal stimulation can influence broader, deeper structures. Furthermore, we examined how intrinsic network dynamics modulate the effectiveness of stimulation, and whether targeting sensory areas at specific frequencies produces patterns of neural activity consistent with those observed in empirical EEG recordings.

3. Results

3.1. Neurostimulation is frequency- and site- dependent

We systematically stimulated each of the model's 90 cortical nodes individually (each corresponding to a region in the AAL90 parcellation scheme [91]) at the frequencies of the five oscillatory modes shown in Figure 1, using coupling and delay parameters $\{K, \mathrm{MD}\}$ corresponding to the network's state of maximum metastability, as quantified by spectral entropy [90]. Weighted degree emerged as the graph metric most strongly correlated with the number of entrained nodes, indicating its relevance as a marker of regional susceptibility to stimulation. The relationship between graph-theoretical features and stimulation spread is further explored in Supplementary Figure S4. From the simulation results, we selected three representative nodes—right precuneus, left precentral gyrus, and right paracentral lobule—which respectively exhibit the highest, intermediate, and lowest weighted degree in the structural connectivity network.

Periodic stimulation consistently induced entrainment at the targeted brain region and often propagated to adjacent brain regions. The magnitude and spatial extent of entrainment varied as a function of both stimulation frequency and the stimulation site, as is shown in Figure 2. At lower stimulation frequencies, entrainment of the right precuneus propagated bilaterally to the occipital, dorsomedial parietal, and medial frontal cortices, with the spatial extent of entrainment progressively decreasing with increasing stimulation frequency. Distinct neural subnetworks were also selectively engaged when stimulating the precentral gyrus at different frequencies; however, entrainment exhibited a weaker relationship with stimulation frequency in terms of propagation pattern.

Unlike the trends described above, low-frequency stimulation failed to induce entrainment in the paracentral lobule, where oscillatory activity was only evident at frequencies exceeding 40 Hz and did not propagate to neighboring brain areas. Figures S5–S9 provide a detailed breakdown of entrainment outcomes across different frequencies at the point of maximum entropy.

To expand on this result, we analyzed whether synchrony at the driving frequency could propagate through the network, entraining nodes beyond those directly connected to the stimulated region—including deep cortical and subcortical structures. Specifically, we examined the patterns of entrainment propagation at 13 Hz, 29.4 Hz, and 43.0 Hz, identifying nodes that became entrained despite lacking direct structural connections to the stimulation site.

Figure 3 and Figure S10 demonstrate that frequency-dependent neural entrainment can propagate to remote nodes not structurally directly connected to the stimulation site, suggesting that rhythmic input influences network activity through indirect pathways mediated by entrained intermediary nodes.

This propagation was particularly evident at 13 Hz, where stimulation engaged widespread cortical and subcortical regions, consistent with the role of low-frequency rhythms in long-range communication. In contrast, higher-frequency stimulation at 29.4 Hz and 43 Hz produced more localized effects, largely restricted within the same hemisphere. Some cortical nodes, such as the left and right precuneus, exhibited a greater capacity to entrain distant regions, reflecting

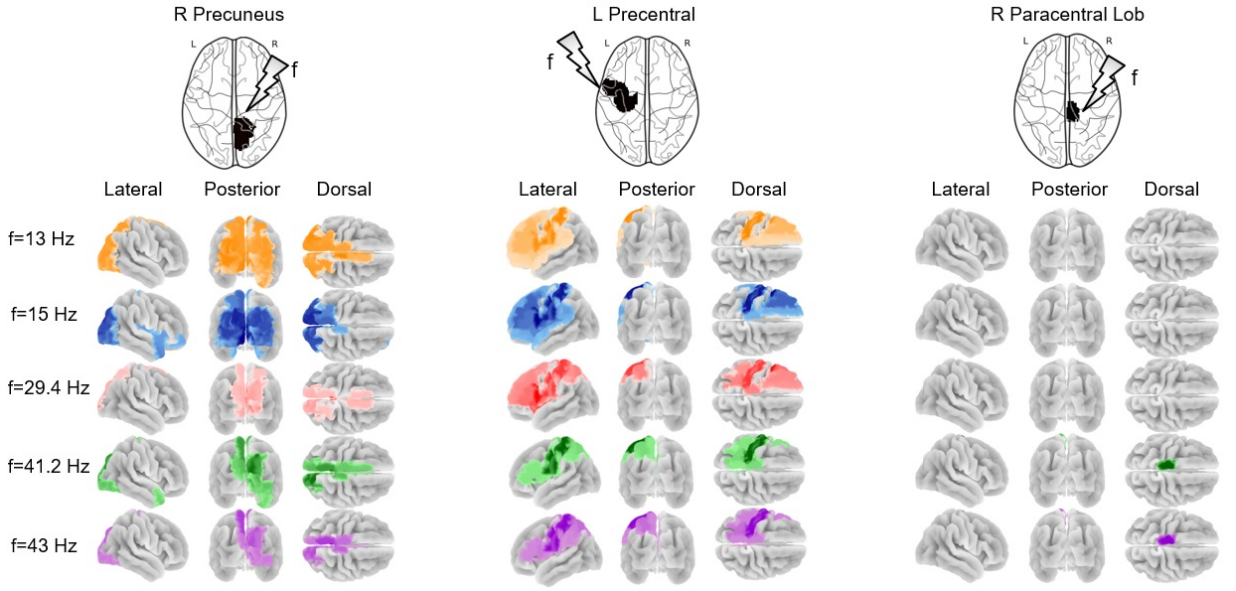

Figure 2: Network selectivity by frequency- and site-dependent neurostimulation. Using the forced Kuramoto network model, cortical nodes with either high (right precuneus), intermediate (left precentral gyrus), or low (right paracentral lobule) Weighted Degree were stimulated at each of the five oscillatory modes that emerge from the brain network model with parameters $\{K, \text{MD}\} = \{4, 21 \text{ ms}\}$ corresponding to the maximum metastability. Functional networks that synchronise to the driving force depend on the frequency and application site, such that selective network modulation could be achieved by the choice of stimulation parameters.

their central role in network connectivity. This frequency selectivity aligns with prior research showing that lower-frequency oscillations facilitate long-range communication, while higher frequencies tend to remain more localized within cortical circuits [14, 17, 29].

These findings highlight that the responsiveness of large-scale brain networks to rhythmic stimulation is shaped by their intrinsic structural and oscillatory properties. Rather than spreading uniformly, external rhythms resonate with the network's natural dynamics, propagating more efficiently along structurally and functionally aligned pathways. Certain frequencies may be inherently better suited to engage specific networks, while others dissipate more quickly and remain localized. Moreover, the extent to which rhythmic input reaches deeper brain structures (see Figure S10) depends not only on the stimulation frequency but also on the topological location of the stimulated node within the network.

3.2. Neurostimulation is structural-connectivity-dependent

Interindividual variability in the spectral features of real neuroimaging data maps onto a range of $\{K, \text{MD}\}$ pairs (Figure 1) of the Kuramoto oscillator model. To investigate how these differences influence network responsiveness, we examined the spread of entrainment as a function of stimulation frequency and $\{K, \text{MD}\}$ pairs, using the right precuneus (the node with the maximum weighted degree) as the stimulation site. The $\{K, \text{MD}\}$ pairs were chosen to reflect those associated with healthy individuals, as illustrated in Figure1.

Using $\{K, \text{MD}\}$ pairs distinct from that associated with maximum metastability reproduced the principal finding observed under the maximally metastable condition illustrated in Figure1. Specifically, the broadest spread of entrainment consistently occurred at the lowest stimulation frequency, regardless of the selected $\{K, \text{MD}\}$ combination, as shown in Figure 4. Furthermore, each stimulation frequency entrained a core subnetwork, which remained stable across $\{K, \text{MD}\}$ combinations. At a stimulation frequency of 13 Hz, this core subnetwork comprised the majority of the occipital brain regions along with large portions of the parietal, cingulate, and limbic cortices in both hemispheres. When the stimulation frequency increased to 29.4 Hz, the core subnetwork was reduced to the bilateral precuneus, the right superior parietal lobe, and the right middle cingulum. At 43 Hz, only the right precuneus remained consistently

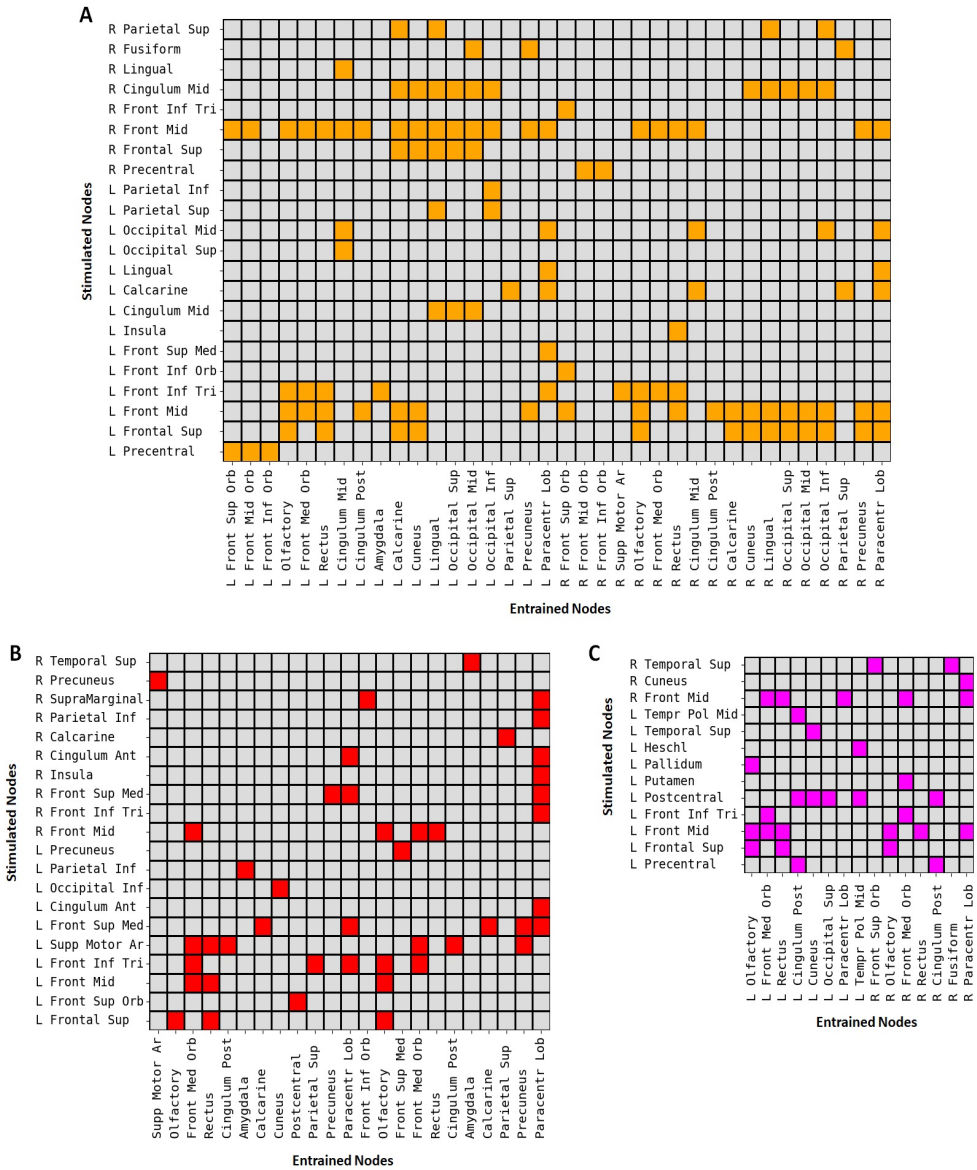

Figure 3: Frequency-dependent propagation of neural entrainment. Each panel shows the relationship between stimulated nodes (Y-axis) and indirectly entrained nodes (X-axis) at 13 Hz (A), 29.4 Hz (B), and 43 Hz (C), using the parameter set corresponding to maximum metastability ($\{K, \mathrm{MD}\} = 4$, 21 ms). Entrained nodes are not directly connected to the stimulated regions but synchronize at the driving frequency. Stimulation at 13 Hz resulted in broader network propagation, while 29.4 Hz and 43 Hz induced more localized entrainment patterns.

activated across all $\{K, \mathrm{MD}\}$ pairs. The spread of entrainment beyond these core subnetworks was modulated by the $\{K, \mathrm{MD}\}$ parameters, as different combinations led to the recruitment of additional nodes and the disengagement of previously participating brain regions as illustrated in Figure 4. Nodes recruited by stimulation included deep cortical brain regions and subcortical structures.

To complement this point, we quantified changes in spectral entropy across brain regions induced by stimulation of the right precuneus, relative to the pre-stimulus baseline (Figure 4B). At a global level, we observed a general reduction in spectral entropy across the network, indicating a shift toward more regular and less variable dynamics in

response to stimulation. For most parameter combinations and frequencies, the number of nodes with decreased spectral entropy was greater than the number with increased spectral entropy, suggesting that stimulation broadly reduced the complexity of local dynamics. This trend is particularly evident at higher stimulation frequencies (e.g., 43 Hz), where the number of nodes with decreased spectral entropy consistently exceeded those with increased spectral entropy, and the overall change in spectral entropy (ΔSE) was markedly negative across all $\{K, \text{MD}\}$ conditions (see Table S2 in Supplementary Material).

These changes were not limited to the directly entrained nodes. Stimulation also modulated the dynamics of non-entrained regions, indicating the propagation of stimulation effects throughout the network. This is consistent with the idea that entrainment leads to a global reorganization of oscillatory activity [56, 65], affecting indirectly connected areas.

However, the specific pattern of spectral entropy modulation varied considerably depending on both stimulation frequency and the structural parameters of the network. There was no clear or consistent relationship between the number of nodes showing increased or decreased spectral entropy and the $\{K, \text{MD}\}$ values. For example, stimulation at 13 Hz resulted in a balanced number of increasing and decreasing spectral entropy in the nodes at K=4, MD=21 ms (45/45), whereas at K=5, MD=19 ms, more nodes showed decreased spectral entropy (59 vs. 31).

The parameter combination corresponding to maximum metastability (K=4, MD=21 ms) generally showed smaller changes in average spectral entropy across frequencies compared to other parameter combinations. This suggests that networks operating near a metastable regime may be more resistant to dynamic reconfiguration, or alternatively, that their intrinsic variability mitigates the effects of further modulation.

3.3. Neurostimulation via sensory-modality-specific frequency entrainment of cortical areas

To validate the findings presented above, we examined whether simulated rhythmic stimulation of sensory cortical regions within the network model could reproduce frequency-dependent entrainment patterns reported in EEG studies of steady-state evoked potentials (SSEPs) and frequency tagging. The stimulation targets—the Calcarine (visual cortex), Heschl's gyrus (auditory cortex), and the Postcentral gyrus (somatosensory cortex)—were selected as representative nodes within modality-specific sensory networks. Stimulation was applied at frequencies corresponding to the endogenous oscillatory range of each respective network. Additionally, multiple $\{K, \text{MD}\}$ sets were used to account for interindividual variability in network dynamics.

Figure 5 and Figure S11 show modality-dependent frequency preferences consistent with prior EEG studies of sensory processing. In the case of the visual cortex (left Calcarine), entrainment was reliably induced across all tested stimulation frequencies and was consistently observed across the full range of $\{K, \text{MD}\}$ combinations. As anticipated, entrainment propagated beyond the stimulation site, often extending to the ipsilateral lateral parietal and temporal cortices, as well as to the contralateral occipital lobe, depending on stimulation frequency and the $\{K, \text{MD}\}$ combination employed in the simulations. It is noteworthy that for every $\{K, \text{MD}\}$ combination, the strongest entrainment was elicited by 13-Hz stimulation.

Similarly, stimulation of the auditory cortex (Heschl's Gyrus) resulted in robust entrainment at all tested frequencies, exhibiting clear frequency-specific patterns. Across all $\{K, \text{MD}\}$ combinations, the most pronounced entrainment was observed at a stimulation frequency of 43 Hz. The broadest spatial propagation of entrainment occurred under simulation parameters of K=5.5, MD=22 ms, encompassing the entire temporal lobe, as well as the lateral parietal and inferior frontal regions. The entrainment also propagated to ipsilateral regions of the stimulated hemisphere.

Entrainment propagation from the somatosensory cortex (Postcentral Gyrus) was typically confined ipsilaterally to the stimulated hemisphere. Depending on the selected $\{K, \text{MD}\}$ combination, the spatial extent of entrainment varied from predominantly frontoparietal regions to more expansive recruitment, including the temporal lobe. Notably, somatosensory entrainment exhibited a less pronounced frequency-specific pattern compared to visual and auditory entrainment. Although no single dominant frequency was observed, the most robust entrainment occurred at stimulation frequencies of 29.4 Hz and 43 Hz.

4. Discussion

This study used a whole-brain network model of coupled forced Kuramoto oscillators to investigate the effects of neurostimulation on oscillatory brain dynamics. We investigated the mechanisms underlying frequency- and site-dependent neurostimulation by systematically varying stimulation parameters, including frequency, target location, and

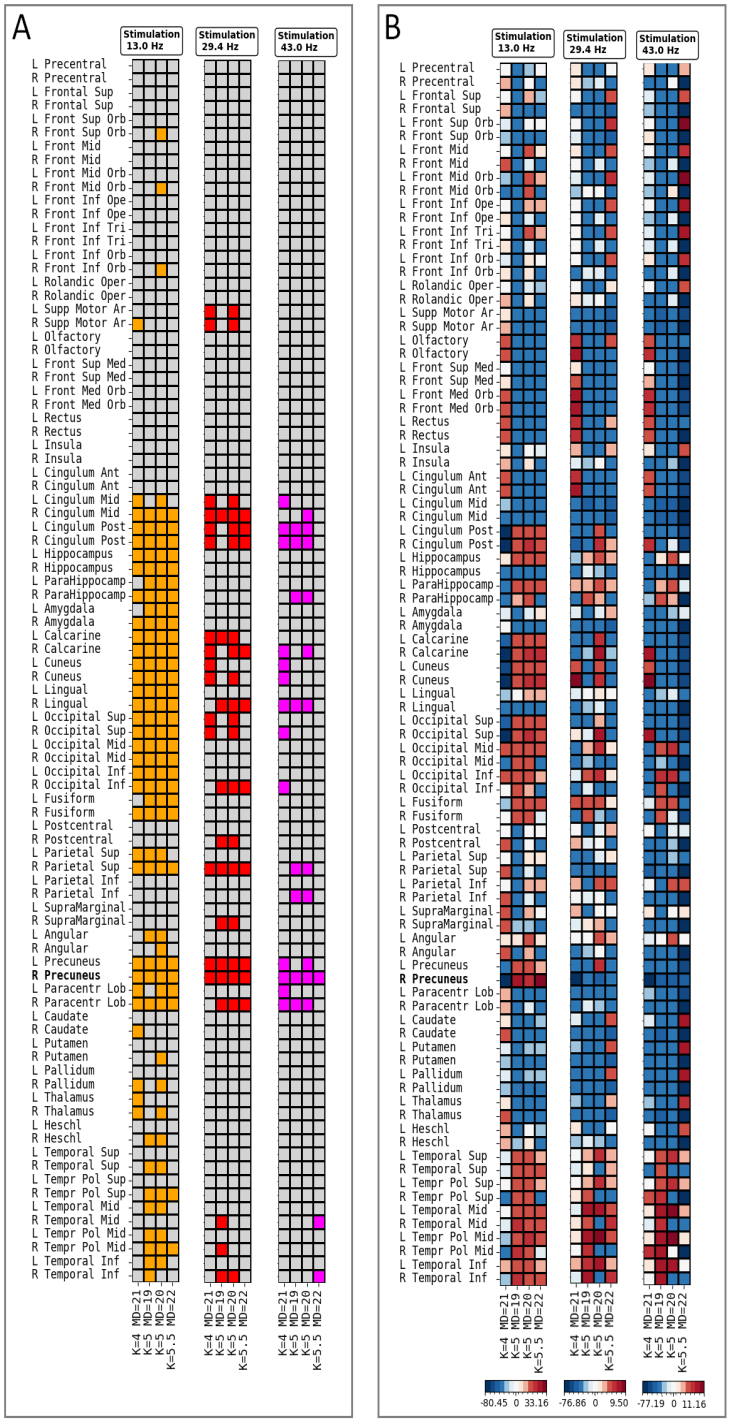

Figure 4: Neurostimulation depends on structural connectivity properties. Effects of 13 Hz, 29.4 Hz, and 43 Hz stimulation of the right precuneus of models with different $\{K, \text{MD}\}$ combinations, corresponding to the healthy subjects in Figure 1. A. The spatial distribution of synchronised networks. While at each frequency a core network is entrained to the driving frequency, there are variations that highlight the (interindividual) structural connectivity dependence. B. Percentage change in spectral entropy relative to pre-stimulation baseline. Neurostimulation induces a reorganization of dynamics both within the directly entrained network and indirectly across the entire system.

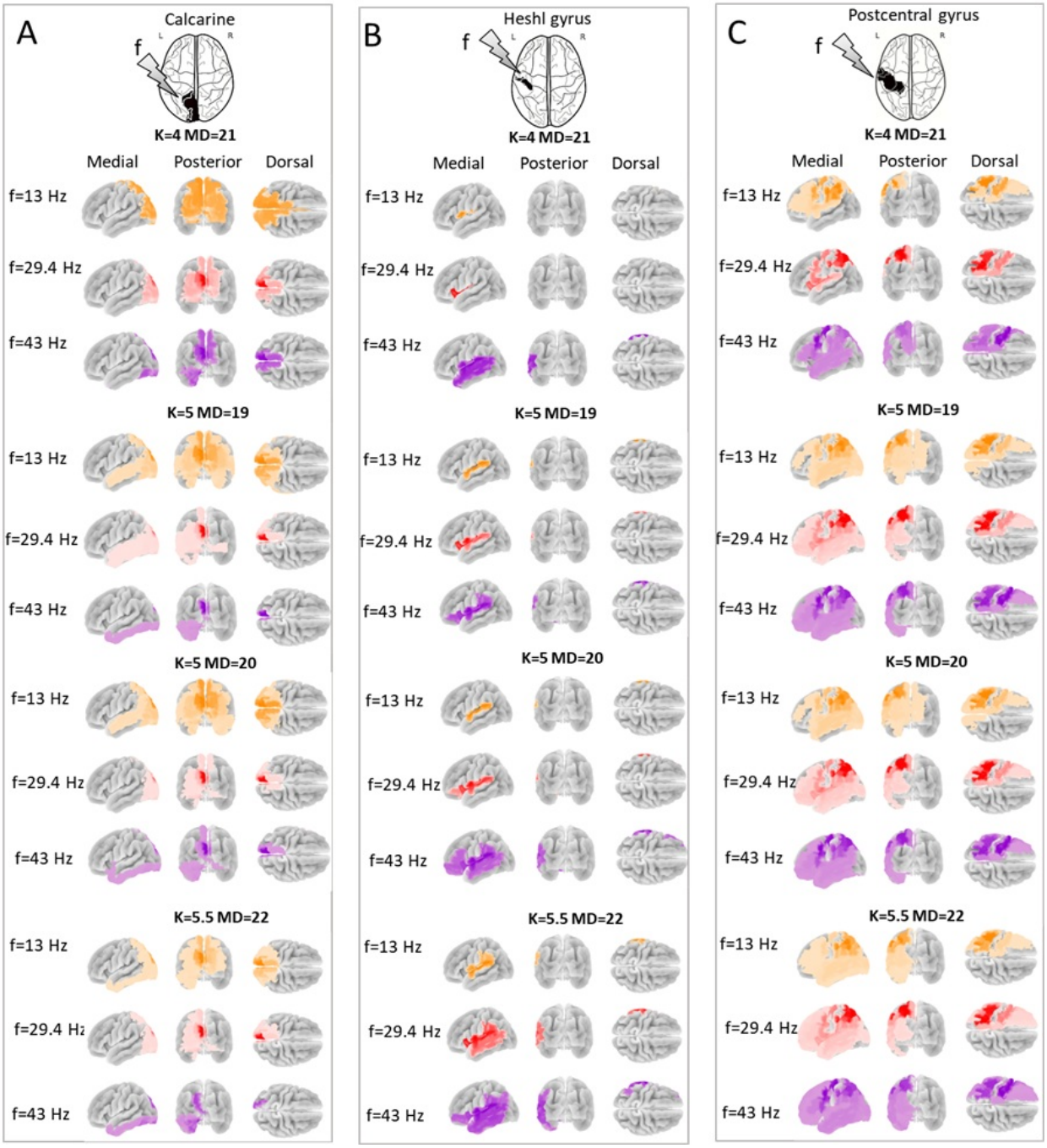

Figure 5: Entrainment effects across sensory cortices as a function of stimulation frequency and structural connectivity properties $\{K, \text{MD}\}$. A. Calcarine (Visual Cortex): Strongest entrainment at 13 Hz, aligning with alpha-band oscillations known to regulate visual processing and attentional gating. B. Heschl's Gyrus (Auditory Cortex): Preferred entrainment at 43 Hz, consistent with gamma-band dominant frequency in auditory networks, reflecting the temporal precision required for auditory processing. C. Postcentral Gyrus (Somatosensory Cortex): No single dominant frequency, but strongest entrainment at 29.4 Hz and 43 Hz, corresponding to beta- and gamma-band activity associated with sensorimotor integration. These findings underscore the role of intrinsic oscillatory dynamics in shaping modality-specific entrainment and demonstrate how neuromodulation effects depend on both regional specialization and individual variability in network state.

intrinsic network properties. The results illustrate that stimulation selectively entrains specific brain regions depending on both frequency and network topology, with higher-degree nodes facilitating broader engagement. Entrainment propagated beyond nodes with direct structural connections in a frequency-dependent manner, with lower frequencies supporting widespread, long-range interactions, whereas higher frequencies tended to produce more localized effects. These findings highlight the significance of structural constraints in neuromodulation and emphasize the importance of individualized stimulation strategies for optimizing therapeutic interventions.

4.1. Role of Stimulation Site in Shaping Entrainment Propagation

Our study highlights the critical role of anatomical specificity in shaping neuromodulation outcomes, emphasizing the structural properties of brain networks as a key determinant of the brain dynamics induced by external stimulation. The frequency-specific propagation of neural entrainment, as illustrated in Figure 2, indicates that certain nodes may serve as effective stimulation sites due to their greater capacity to transmit information to a larger number of downstream brain regions. The network dynamics were contingent upon the connectivity profile of the stimulated nodes, with higher-weighted degree nodes (such as the precuneus) facilitating more extensive network interactions. The modulated neural subnetworks identified here (Figure 2) closely align with the spontaneous frequency-specific networks previously described by Torres et al. (2024) with the exact activated brain subnetworks being contingent upon the stimulation target.

In our study, the largest entrainment spread was associated with stimulation of the precuneus—the node with higher-weighted degree connectivity (Figure 2). The precuneus is considered a central hub of the default mode network (DMN) [32, 37], the largest functional resting-state network. As a hub, the precuneus plays a central role in orchestrating coherent neural activity [37] and promoting integrative brain states [27, 95], associated with self-referential thinking, episodic memory retrieval, and mind-wandering [24]. Dysfunction or structural compromise of the precuneus is associated with neurodegenerative conditions, particularly Alzheimer's disease (AD) [25], such that rTMS targeting the DMN by precuneus stimulation has been suggested as a promising therapeutic approach in AD patients [51].

Our findings indicate that entrainment of the precuneus propagates to regions such as the posterior cingulate gyrus and the hippocampus (Figure 2), key nodes of the DMN which display functional hypoconnectivity in AD [75]. This is consistent with previous research, which indicates that hubs can be effective targets for widespread neuromodulatory interventions. Previous modeling research in neurodegenerative diseases suggests that compromised rich-club organization of the human connectome, resulting from structural impairments of network hubs, generates brain dynamic patterns that resemble those observed in AD and the behavioral variant of frontotemporal dementia (bvFTD) [23]. In this context, in silico perturbations of the oscillatory activity of the precuneus, are key in mediating bidirectional transitions between brain dynamics representative of healthy individuals and dementia patients [23].

4.2. Structural Connectivity Constraints on Neuromodulation

In addition to the local connectivity properties of individual nodes, as quantified by their weighted degree, neuromodulation outcomes are also critically influenced by global model parameters. Our findings demonstrate that systematic variations in global coupling K and mean delay MD of the whole brain model substantially affect neural entrainment (Figure 4). Therefore, while a consistent core subset of nodes exhibited entrainment across individuals, the magnitude and spatial distribution of entrainment varied significantly, reflecting the influence of interindividual differences in structural connectivity patterns. As previously described, the dynamic features observed in real neuroimaging data map onto a range of $\{K, \mathrm{MD}\}$ sets (Figure 1), such that the sets of $\{K, \mathrm{MD}\}$ capture interindividual variability in structural connectivity that give rise to variations in entrainment generation and propagation (Figure 4). In other words, variations in $\{K, \mathrm{MD}\}$ parameters effectively account for structural connectivity differences among individuals, enabling a more customized approach to neuromodulation research and its applications. This finding is consistent with previous studies that indicate structural connectivity parameters $\{K, \mathrm{MD}\}$ serve as effective proxies for real neuroimaging data, capturing essential aspects of intersubject variability [17, 90]. Consequently, incorporating these parameters into neurostimulation frameworks is crucial for understanding and predicting individualized neuromodulatory responses. These results emphasize the extent to which neuromodulation effects are subject-specific and contribute to explaining the observed variability in cognitive and behavioral outcomes when identical stimulation protocols are applied across clinical populations, where substantial variability in structural connectivity is commonly expected [31, 52, 75, 87, 98].

Spectral entropy analyses further revealed that neuromodulation induces widespread reorganization of network dynamics, with effects propagating beyond directly stimulated regions. Importantly, networks operating at maximum

metastability exhibited the least disruption, suggesting that they are more adaptable to external inputs while maintaining functional flexibility. These findings reinforce the notion that neuromodulation efficacy is fundamentally constrained by the brain's structural properties, highlighting the necessity of tailored stimulation strategies that account for individual neuroanatomical differences. Personalized approaches to neuromodulation, informed by structural connectivity data, could optimize intervention outcomes and improve therapeutic efficacy in clinical settings.

4.3. Frequency-Dependent Entrainment Propagation

Our findings indicate that both the generation and propagation of neural entrainment exhibit frequency-dependent characteristics (Figures 2, 3, 4, and 5). These results align well with the principles of oscillatory communication, in which lower-frequency rhythms facilitate long-range cortical interactions, while higher-frequency oscillations are predominantly localized within specific neural circuits [14, 34, 35, 92]. The distinct oscillatory regimes of nodes with different weighted degrees in the mode of maximum metastability (Figure 2), are consistent with the posterior-to-anterior gradient of increasing intrinsic resting-state oscillatory frequencies of the human brain [18].

In our maximum metastability simulations, the lowest tested stimulation frequency (13 Hz) is close to the natural oscillatory frequency of the precuneus, which ranges between 10.2 Hz and 11.4 Hz and lies within the alpha frequency band [18]. This frequency alignment explains the pronounced strength and extensive propagation of the entrainment elicited in the precuneus by the 13 Hz stimulation (Figure 2). Similarly, the robust and widespread propagation of the entrainment elicited by 29.4 Hz stimulation targeting the precentral gyrus (Figure 2) corresponds closely to its intrinsic oscillatory frequency range (21.7–22.7 Hz) [18]. A progressive decrease in the entrainment strength of both regions, accompanied by a reduction in the spatial extent of entrainment propagation, was evident as the stimulation frequency exceeded their intrinsic oscillatory frequencies (Figure 2). Previous studies have typically excluded or inconsistently reported gamma-band activity due to contamination by ocular and myogenic artifacts [18, 21, 38, 63]. These limitations prevented us from conducting a similar analysis for the paracentral lobule. Nevertheless, M/EEG studies have documented gamma-frequency functional connectivity in brain regions anatomically related to the paracentral lobule, such as the primary somatosensory cortex [44]. Notably, a three-year longitudinal EEG study highlighted that gamma-band oscillations have the lowest reliability of test-retest, suggesting that future research may achieve greater consistency focusing on alpha and beta frequencies, which demonstrate higher reliability estimates [60].

Since gamma-activity characterizes the intrinsic oscillatory regimes of individual nodes in our simulations, the emergence of frequency-selective networks (Figures 2, 3, and 4) is fundamentally dependent on the whole-brain network topology, i.e., the brain connectome [15, 90]. Rather than spreading uniformly, rhythmic stimulation appears to resonate with the network's natural dynamics, traveling along paths of least resistance where structural connectivity and oscillatory properties facilitate its transmission. Some frequencies may be inherently better suited to engaging specific networks, while others encounter more dissipation and remain spatially constrained. This insight is relevant for the development of frequency-specific stimulation strategies aimed at restoring disrupted brain dynamics in neurological conditions characterized by frequency-dependent functional connectivity impairments. This is the case for mental health disorders such as schizophrenia and neurodegenerative diseases such as AD. M/EEG investigations in schizophrenia have documented abnormalities in both local and long-range oscillatory network dynamics across multiple frequency bands, although methodological limitations have led to some inconsistencies in the literature [3]. In contrast, more robust findings have been reported in AD, where systematic posterior hypoconnectivity in the alpha and beta frequency bands has been consistently observed [6, 10, 70, 75, 80]. Frequency-specific stimulation of key cortical hubs may facilitate indirect modulation of distant or deep-brain structures (see Figure S10), offering significant potential advantages for the development of non-invasive therapeutic protocols.

4.4. Sensory-Modality-Specific Frequency Entrainment

The natural oscillatory mode of the calcarine sulcus and surrounding cortex that characterizes the metastability state of our whole brain model of Kuramoto coupled oscillators is dominated by 13 Hz oscillations [90]. This frequency closely aligns with the intrinsic oscillatory profile identified for this brain region through empirical M/EEG recordings, where alpha oscillations constitute approximately one-third of its total oscillatory activity [18]. Similarly, frequencies near or exceeding 30 Hz dominate the resting-state intrinsic oscillatory mode of Heschl's gyrus within the metastable state of the Kuramoto oscillator-based whole-brain model mentioned above [90]. In view of this evidence, our results illustrate that, in the simulated brain, external rhythmic stimulation effectively interacts with the intrinsic frequency preferences of sensory cortical areas, modulating their endogenous oscillatory dynamics in a

manner consistent with empirical M/EEG observations (Figure 5), which aligns with previous computational studies on neural entrainment [71]. Therefore, our study bridges computational modeling outcomes to well-established literature on steady-state evoked potentials (SSEPs), frequency tagging, and modality-specific sensory entrainment. Specifically, the observed preference of the visual cortex for 13 Hz stimulation in our simulations aligns with extensive research on alpha-band entrainment (e.g., [85]), while the robust auditory cortical response observed at 43 Hz corresponds with previously documented gamma-band responses elicited by auditory stimulation (e.g., [89]. Additionally, the relatively weaker frequency selectivity observed within the somatosensory cortex in our simulations (Figure 5) can be interpreted in the context of previous research documenting beta- and gamma-band coherence during somatosensory processing [83]. These connections further validate our model by demonstrating consistency with established findings in neuromodulation using sensory stimulation.

The parameters that modulate structural connectivity in our model K, MD, which were varied in our study to represent interindividual variability, were found to significantly influence the spatial extent of entrainment (Figures 4 and 5). This finding reinforces previous computational studies suggesting that the propagation of entrainment is contingent upon the coupling strength between brain areas and the correspondence between their intrinsic oscillatory frequencies [71]. The variability in entrainment propagation (Figures 4 and 5) highlights the potential benefit of incorporating individual structural and dynamical constraints into effective frequency tuning for personalized neuromodulation, thereby enhancing neuromodulation efficacy.

Collectively, these results underscore the importance of frequency selection in non-invasive brain stimulation protocols. The alignment between our model-derived entrainment patterns and established EEG signatures supports the use of computational approaches to predict optimal stimulation frequencies for targeting specific brain regions. By leveraging insights from SSEP and frequency tagging paradigms, future research can refine neuromodulation strategies to enhance sensory processing and cognitive function in both healthy and clinical populations.

4.5. Implications for Non-Invasive Neuromodulation

Our findings have important implications for optimizing non-invasive neuromodulation techniques such as rTMS and tACS. By aligning stimulation parameters with the natural oscillatory preferences of targeted networks, it may be possible to enhance intervention specificity and efficacy. Moreover, the observed variability in neuromodulation responses underscores the necessity of individualized approaches, leveraging neuroimaging and computational modeling to tailor stimulation protocols based on each subject's structural and functional architecture. Future research should focus on translating these principles into clinical applications, particularly for populations where structural connectivity differences may influence therapeutic outcomes.

5. Future Directions

While our current model effectively captures frequency- and site-specific dynamics of neurostimulation, some limitations point to important directions for future research. First, this work primarily focuses on direct entrainment at specific frequencies but does not account for cross-frequency interactions, such as low-frequency stimulation modulating high-frequency activity. These interactions are widely studied in neural oscillations and have been shown to shape large-scale communication and cognitive integration across brain networks [1, 49, 81, 97]. Future extensions of the model should incorporate mechanisms of phase-amplitude coupling and nested oscillations to evaluate how stimulation at one frequency may influence neural activity across other frequency bands, potentially enhancing cognitive or therapeutic outcomes.

Second, although we used different combinations of $\{K, \mathrm{MD}\}$ parameters as a proxy to capture inter-individual variability in baseline dynamics, the simulations were based on a population-average structural connectome, which does not fully account for anatomical differences across individuals. Incorporating individualized connectomes would enhance the biological realism of the model and improve its capacity to predict subject-specific responses to neurostimulation.

Finally, our model does not currently include mechanisms of plasticity, limiting its applicability to short-term entrainment effects and preventing it from modeling the long-term neuroadaptive changes induced by repeated or chronic stimulation. Plasticity plays a crucial role in sustaining therapeutic outcomes in clinical contexts where repetitive neuromodulation can induce lasting network reorganization [2, 30, 40, 82]. Incorporating plasticity mechanisms would enable estimation of dose-dependent effects and allow exploration of how various stimulation parameters contribute to long-term behavioral change. This addition would enhance the model's relevance for real-world therapeutic

interventions, where cumulative stimulation protocols are commonly used to promote durable neurophysiological improvements.

5.1. Clinical Applications

While our findings advance the mechanistic understanding of how rhythmic neurostimulation interacts with large-scale brain dynamics, more research and validation are necessary to translate these insights into clinical applications. A substantial body of evidence has linked dysfunctional brain circuits and oscillatory networks to the pathophysiology of numerous neurological and psychiatric disorders [22, 28, 62, 64, 66, 69, 93]. The specific frequency-site combinations identified in this study's model could guide the development of more personalized and effective neuromodulation interventions. Such approaches would go beyond conventional protocols that apply fixed-frequency stimulation without accounting for individual differences in brain network organization or oscillatory dynamics. Instead, future therapies could be adapted to selectively engage functionally relevant circuits based on specific therapeutic goals or task demands, offering a more precise and flexible alternative to traditional neuromodulatory methods.

Model-based neuromodulation could leverage computational analyses to optimize stimulation parameters, aligning interventions with individual oscillatory rhythms to enhance efficacy and minimize side effects. For example, 13 Hz stimulation of the visual cortex may help restore alpha oscillatory function in disorders such as migraine with aura or visual snow syndrome, where alpha-band dysfunction has been reported [46, 50]. Similarly, 43 Hz auditory cortex stimulation could benefit auditory processing disorders and schizophrenia, where gamma-band abnormalities are present [67, 88]. Furthermore, beta/gamma stimulation of the somatosensory cortex may support rehabilitation strategies for stroke and Parkinson's disease, conditions characterized by impaired beta/gamma coherence [41, 73, 77, 86].

Integrating computational modeling, personalized oscillatory entrainment, and real-time neurofeedback would provide a pathway toward more effective, individualized neuromodulation therapies. Future interventions based on these approaches have the potential to significantly improve treatment outcomes for a range of neurological and psychiatric disorders.

6. Conclusions

This study demonstrates the potential of using a whole brain network model of coupled Kuramoto oscillators to simulate the effects of periodic stimulation on large-scale brain networks. By exploring frequency-dependent entrainment and propagation dynamics, we identified the critical role of stimulation parameters, such as frequency and target location, in modulating neural activity. Furthermore, we show that entrainment propagates beyond directly connected nodes, suggesting that indirect pathways play a key role in entrainment. These insights provide a foundation for optimizing non-invasive neuromodulation strategies, paving the way for more personalized and effective clinical interventions. Specifically, tailoring stimulation frequency and target location to individual network properties could enhance neurostimulation protocols for neurological and psychiatric treatments. Future research should explore adaptive stimulation techniques that dynamically adjust parameters based on real-time EEG feedback, potentially improving therapeutic outcomes and patient-specific interventions.

7. Funding

This research was supported by ANID, Chile: FONDECYTs Iniciación 11241484 (MO), Postdoctorado 3230682 (FAT), Regular 1231132 (AW), 1221665 (PG), 1241695 (WED); Exploración 13240042 (MO), 13240064 (WED); Anillo ACT210053, and BASALs FB210008, AFB240002.

CRediT authorship contribution statement

Mónica Otero: Conceptualization, Methodology, Validation, Formal analysis, Investigation, Writing -original draft. **Elida Poo:** Methodology, Software, Validation, Formal analysis, Investigation, Writing -original draft. **Felipe Torres:** Methodology, Software, Validation, Formal analysis, Writing - review & editing. **Cristobal Mendoza:** Software, Validation, Formal analysis. **Caroline Lea-Carnall:** Methodology, Validation, Investigation, Writing - review & editing. **Alejandro Weinstein:** Methodology, Validation, Formal analysis, Writing - review & editing. **Pamela Guevara:** Methodology, Validation, Formal analysis, Writing - review & editing. **Pavel Prado:** Methodology,

Validation, Formal analysis, Investigation, Writing - review & editing. **Joana Cabral:** Methodology, Investigation, Writing - review & editing. **Wael El-Deredy:** Conceptualization, Methodology, Validation, Formal analysis, Investigation, Writing - review & editing.

During the preparation of this manuscript, the authors used Grammarly to assist in improving language and readability of the text. After using this tool, the authors reviewed and edited the content as needed and take full responsibility for the content of the publication.

References

[1] Abubaker, M., Al Qasem, W., Kvašňák, E., 2021. Working memory and cross-frequency coupling of neuronal oscillations. Frontiers in psychology 12, 756661.

[2] Agboada, D., Zhao, Z., Wischnewski, M., 2025. Neuroplastic effects of transcranial alternating current stimulation (tacs): from mechanisms to clinical trials. Frontiers in Human Neuroscience 19, 1548478.

[3] Alamian, G., Hincapié, A.S., Pascarella, A., Thiery, T., Combrisson, E., Saive, A.L., Martel, V., Althukov, D., Haesebaert, F., Jerbi, K., 2017. Measuring alterations in oscillatory brain networks in schizophrenia with resting-state meg: State-of-the-art and methodological challenges. Clinical Neurophysiology 128, 1719–1736.

[4] Alexander, M.L., Alagapan, S., Lugo, C.E., Mellin, J.M., Lustenberger, C., Rubinow, D.R., Fröhlich, F., 2019. Double-blind, randomized pilot clinical trial targeting alpha oscillations with transcranial alternating current stimulation (tacs) for the treatment of major depressive disorder (mdd). Translational psychiatry 9, 106.

[5] Aydore, S., Pantazis, D., Leahy, R.M., 2013. A note on the phase locking value and its properties. NeuroImage 74, 231–244.

[6] Babiloni, C., Lizio, R., Marzano, N., Capotosto, P., Soricelli, A., Triggiani, A.I., Cordone, S., Gesualdo, L., Del Percio, C., 2016. Brain neural synchronization and functional coupling in alzheimer's disease as revealed by resting state eeg rhythms. International Journal of Psychophysiology 103, 88–102.

[7] Barr, M.S., Farzan, F., Arenovich, T., Chen, R., Fitzgerald, P.B., Daskalakis, Z.J., 2011. The effect of repetitive transcranial magnetic stimulation on gamma oscillatory activity in schizophrenia. PloS one 6, e22627.

[8] Başar, E., Başar-Eroğlu, C., Karakaş, S., Schürmann, M., 2000. Brain oscillations in perception and memory. International journal of psychophysiology 35, 95–124.

[9] Behrens, T.E., Woolrich, M.W., Jenkinson, M., Johansen-Berg, H., Nunes, R.G., Clare, S., Matthews, P.M., Brady, M., Smith, S.M., 2003. Characterization and propagation of uncertainty in diffusion-weighted mr imaging. Magnetic Resonance in Medicine 50, 1077–1088. doi:10.1002/mrm.10609.

[10] Briels, C.T., Schoonhoven, D.N., Stam, C.J., de Waal, H., Scheltens, P., Gouw, A.A., 2020. Reproducibility of eeg functional connectivity in alzheimer's disease. Alzheimer's research & therapy 12, 1–14.

[11] Brinkman, B.A., Yan, H., Maffei, A., Park, I.M., Fontanini, A., Wang, J., La Camera, G., 2022. Metastable dynamics of neural circuits and networks. Applied Physics Reviews 9.

[12] Buzsáki, G., 2006. Rhythms of the Brain. Oxford university press.

[13] Buzsáki, G., Anastassiou, C.A., Koch, C., 2012. The origin of extracellular fields and currents—eeg, ecog, lfp and spikes. Nature reviews neuroscience 13, 407–420.

[14] Buzsáki, G., Draguhn, A., 2004. Neuronal oscillations in cortical networks. Science 304, 1926–1929. doi:10.1126/science.1099745.

[15] Cabral, J., Castaldo, F., Vohryzek, J., Litvak, V., Bick, C., Lambiotte, R., Friston, K., Kringelbach, M.L., Deco, G., 2022. Metastable oscillatory modes emerge from synchronization in the brain spacetime connectome. Communications Physics 5, 184.

[16] Cabral, J., Hugues, E., Sporns, O., Deco, G., 2011. Role of local network oscillations in resting-state functional connectivity. Neuroimage 57, 130–139.

[17] Cabral, J., Luckhoo, H., Woolrich, M., Joensson, M., Mohseni, H., Baker, A., Kringelbach, M.L., Deco, G., 2014. Exploring mechanisms of spontaneous functional connectivity in meg: how delayed network interactions lead to structured amplitude envelopes of band-pass filtered oscillations. Neuroimage 90, 423–435.

[18] Capilla, A., Arana, L., García-Huéscar, M., Melcón, M., Gross, J., Campo, P., 2022. The natural frequencies of the resting human brain: An meg-based atlas. NeuroImage 258, 119373.

[19] Castaldo, F., Páscoa dos Santos, F., Timms, R.C., Cabral, J., Vohryzek, J., Deco, G., Woolrich, M., Friston, K., Verschure, P., Litvak, V., 2023. Multi-modal and multi-model interrogation of large-scale functional brain networks. NeuroImage 277, 120236.

[20] Castro, S., El-Deredy, W., Battaglia, D., Orio, P., 2020. Cortical ignition dynamics is tightly linked to the core organisation of the human connectome. PLOS Computational Biology 16, 1–23. doi:10.1371/journal.pcbi.1007686.

[21] Chen, A.C., Feng, W., Zhao, H., Yin, Y., Wang, P., 2008. Eeg default mode network in the human brain: spectral regional field powers. Neuroimage 41, 561–574.

[22] Colmers, P.L., Maguire, J., 2020. Network dysfunction in comorbid psychiatric illnesses and epilepsy. Epilepsy Currents 20, 205–210.

[23] Coronel-Oliveros, C., Gómez, R.G., Ranasinghe, K., Sainz-Ballesteros, A., Legaz, A., Fittipaldi, S., Cruzat, J., Herzog, R., Yener, G., Parra, M., et al., 2024. Viscous dynamics associated with hypoexcitation and structural disintegration in neurodegeneration via generative whole-brain modeling. Alzheimer's & Dementia 20, 3228–3250.

[24] Dadario, N.B., Sughrue, M.E., 2023. The functional role of the precuneus. Brain 146, 3598–3607.

[25] De Haan, W., Mott, K., Van Straaten, E.C., Scheltens, P., Stam, C.J., 2012. Activity dependent degeneration explains hub vulnerability in alzheimer's disease. PLoS Comput Biol 8.

[26] Deco, G., Jirsa, V., McIntosh, A.R., Sporns, O., Kötter, R., 2009. Key role of coupling, delay, and noise in resting brain fluctuations. Proceedings of the National Academy of Sciences 106, 10302–10307.

[27] Deco, G., Van Hartevelt, T.J., Fernandes, H.M., Stevner, A., Kringelbach, M.L., 2017. The most relevant human brain regions for functional connectivity: Evidence for a dynamical workspace of binding nodes from whole-brain computational modelling. Neuroimage 146, 197–210.

[28] Dong, D., Wang, Y., Chang, X., Luo, C., Yao, D., 2018. Dysfunction of large-scale brain networks in schizophrenia: a meta-analysis of resting-state functional connectivity. Schizophrenia bulletin 44, 168–181.

[29] Ermentrout, G.B., Kleinfeld, D., 2001. Traveling electrical waves in cortex: insights from phase dynamics and speculation on a computational role. Neuron 29, 33–44.

[30] Fitzsimmons, S.M., Oostra, E., Postma, T.S., van der Werf, Y.D., van den Heuvel, O.A., 2024. Repetitive transcranial magnetic stimulation–induced neuroplasticity and the treatment of psychiatric disorders: State of the evidence and future opportunities. Biological Psychiatry 95, 592–600.

[31] Fox, M.D., Buckner, R.L., Liu, H., Chakravarty, M.M., Lozano, A.M., Pascual-Leone, A., 2014. Resting-state networks link invasive and noninvasive brain stimulation across diverse psychiatric and neurological diseases. Proceedings of the National Academy of Sciences 111, E4367–E4375.

[32] Fox, M.D., Raichle, M.E., 2007. Spontaneous fluctuations in brain activity observed with functional magnetic resonance imaging. Nature reviews neuroscience 8, 700–711.

[33] Freeman, L., 1977. A set of measures of centrality based on betweenness. Sociometry 40, 35–41.

[34] Fries, P., 2005. A mechanism for cognitive dynamics: neuronal communication through neuronal coherence. Trends in cognitive sciences 9, 474–480.

[35] Fries, P., 2015. Rhythms for cognition: communication through coherence. Neuron 88, 220–235.

[36] Fries, P., Reynolds, J.H., Rorie, A.E., Desimone, R., 2001. Modulation of oscillatory neuronal synchronization by selective visual attention. Science 291, 1560–1563.

[37] Griffa, A., Van Den Heuvel, M.P., 2018. Rich-club neurocircuitry: function, evolution, and vulnerability. Dialogues in clinical neuroscience 20, 121–132.

[38] Groppe, D.M., Bickel, S., Keller, C.J., Jain, S.K., Hwang, S.T., Harden, C., Mehta, A.D., 2013. Dominant frequencies of resting human brain activity as measured by the electrocorticogram. Neuroimage 79, 223–233.

[39] Grover, S., Nguyen, J.A., Reinhart, R.M., 2021. Synchronizing brain rhythms to improve cognition. Annual review of medicine 72, 29–43.

[40] Grover, S., Wen, W., Viswanathan, V., Gill, C.T., Reinhart, R.M., 2022. Long-lasting, dissociable improvements in working memory and long-term memory in older adults with repetitive neuromodulation. Nature neuroscience 25, 1237–1246.

[41] Guerra, A., Asci, F., D'Onofrio, V., Sveva, V., Bologna, M., Fabbrini, G., Berardelli, A., Suppa, A., 2020. Enhancing gamma oscillations restores primary motor cortex plasticity in parkinson's disease. Journal of Neuroscience 40, 4788–4796.

[42] Helakari, H., Korhonen, V., Holst, S.C., Piispala, J., Kallio, M., Väyrynen, T., Huotari, N., Raitamaa, L., Tuunanen, J., Kananen, J., et al., 2022. Human nrem sleep promotes brain-wide vasomotor and respiratory pulsations. Journal of Neuroscience 42, 2503–2515.

[43] Hellyer, P.J., Scott, G., Shanahan, M., Sharp, D.J., Leech, R., 2015. Cognitive flexibility through metastable neural dynamics is disrupted by damage to the structural connectome. Journal of Neuroscience 35, 9050–9063.

[44] Hillebrand, A., Barnes, G.R., Bosboom, J.L., Berendse, H.W., Stam, C.J., 2012. Frequency-dependent functional connectivity within resting-state networks: an atlas-based meg beamformer solution. Neuroimage 59, 3909–3921.

[45] Hinchliffe, C., Yogarajah, M., Elkommos, S., Tang, H., Abasolo, D., 2022. Entropy measures of electroencephalograms towards the diagnosis of psychogenic non-epileptic seizures. Entropy 24, 1348.

[46] van den Hoek, T.C., Perenboom, M.J., Terwindt, G.M., Tolner, E.A., van de Ruit, M., 2024. Bi-sinusoidal light stimulation reveals an enhanced response power and reduced phase coherence at the visual cortex in migraine. Frontiers in Neurology 14, 1274059.

[47] Huang, Y., Zelmann, R., Hadar, P., Dezha-Peralta, J., Richardson, R.M., Williams, Z.M., Cash, S.S., Keller, C.J., Paulk, A.C., 2024. Theta-burst direct electrical stimulation remodels human brain networks. Nature Communications 15, 6982.

[48] Inouye, T., Shinosaki, K., Sakamoto, H., Toi, S., Ukai, S., Iyama, A., Katsuda, Y., Hirano, M., 1991. Quantification of eeg irregularity by use of the entropy of the power spectrum. Electroencephalography and clinical neurophysiology 79, 204–210.

[49] Kim, S.E., Kim, H.S., Kwak, Y., Ahn, M.H., Choi, K.M., Min, B.K., 2022. Neurodynamic correlates for the cross-frequency coupled transcranial alternating current stimulation during working memory performance. Frontiers in Neuroscience 16, 1013691.

[50] Klein, A., Aeschlimann, S.A., Zubler, F., Scutelnic, A., Riederer, F., Ertl, M., Schankin, C.J., 2024. Alterations of the alpha rhythm in visual snow syndrome: a case-control study. The journal of headache and pain 25, 53.

[51] Koch, G., Casula, E.P., Bonnì, S., Borghi, I., Assogna, M., Minei, M., Pellicciari, M.C., Motta, C., D'Acunto, A., Porrazzini, F., et al., 2022. Precuneus magnetic stimulation for alzheimer's disease: a randomized, sham-controlled trial. Brain 145, 3776–3786.

[52] Konrad, K., Eickhoff, S.B., 2010. Is the adhd brain wired differently? a review on structural and functional connectivity in attention deficit hyperactivity disorder. Human brain mapping 31, 904–916.

[53] Kucewicz, M.T., Berry, B.M., Kremen, V., Brinkmann, B.H., Sperling, M.R., Jobst, B.C., Gross, R.E., Lega, B., Sheth, S.A., Stein, J.M., et al., 2017. Dissecting gamma frequency activity during human memory processing. Brain 140, 1337–1350.

[54] Kuramoto, Y., 1975. Self-entrainment of a population of coupled non-linear oscillators, in: International Symposium on Mathematical Problems in Theoretical Physics: January 23–29, 1975, Kyoto University, Kyoto/Japan, Springer. pp. 420–422.

[55] Kurtin, D.L., Giunchiglia, V., Vohryzek, J., Cabral, J., Skeldon, A.C., Violante, I.R., 2023. Moving from phenomenological to predictive modelling: Progress and pitfalls of modelling brain stimulation in-silico. Neuroimage 272, 120042.

[56] Lakatos, P., Gross, J., Thut, G., 2019. A new unifying account of the roles of neuronal entrainment. Current Biology 29, R890–R905.

[57] Landau, L.D., 1944. On the problem of turbulence, in: Dokl. Akad. Nauk USSR, p. 311.

[58] Lea-Carnall, C.A., Montemurro, M.A., Trujillo-Barreto, N.J., Parkes, L.M., El-Deredy, W., 2016a. Cortical resonance frequencies emerge from network size and connectivity. PLoS computational biology 12, e1004740.

[59] Lea-Carnall, C.A., Montemurro, M.A., Trujillo-Barreto, N.J., Parkes, L.M., El-Deredy, W., 2016b. Cortical resonance frequencies emerge from network size and connectivity. PLOS Computational Biology 12, 1–19. doi:10.1371/journal.pcbi.1004740.

[60] Lew, B.J., Fitzgerald, E.E., Ott, L.R., Penhale, S.H., Wilson, T.W., 2021. Three-year reliability of meg resting-state oscillatory power. Neuroimage 243, 118516.
[61] Lin, J., 1991. Divergence measures based on the shannon entropy. IEEE Transactions on Information theory 37, 145–151.
[62] Lindquist, B.E., Timbie, C., Voskobiynyk, Y., Paz, J.T., 2023. Thalamocortical circuits in generalized epilepsy: Pathophysiologic mechanisms and therapeutic targets. Neurobiology of disease 181, 106094.
[63] Mahjoory, K., Schoffelen, J.M., Keitel, A., Gross, J., 2020. The frequency gradient of human resting-state brain oscillations follows cortical hierarchies. elife 9, e53715.
[64] McCarthy, H., Skokauskas, N., Mulligan, A., Donohoe, G., Mullins, D., Kelly, J., Johnson, K., Fagan, A., Gill, M., Meaney, J., et al., 2013. Attention network hypoconnectivity with default and affective network hyperconnectivity in adults diagnosed with attention-deficit/hyperactivity disorder in childhood. JAMA psychiatry 70, 1329–1337.
[65] Menétrey, M.Q., Pascucci, D., 2024. Spectral tuning and after-effects in neural entrainment. Behavioral and Brain Functions 20, 29.
[66] Menon, V., 2023. 20 years of the default mode network: A review and synthesis. Neuron 111, 2469–2487.
[67] Metzner, C., Mäki-Marttunen, T., Karni, G., McMahon-Cole, H., Steuber, V., 2022. The effect of alterations of schizophrenia-associated genes on gamma band oscillations. Schizophrenia 8, 46.
[68] Moreira, C.A., de Aguiar, M.A., 2019. Global synchronization of partially forced kuramoto oscillators on networks. Physica A: Statistical Mechanics and its Applications 514, 487–496.
[69] Norman, L.J., Sudre, G., Price, J., Shastri, G.G., Shaw, P., 2023. Evidence from "big data" for the default-mode hypothesis of adhd: a mega-analysis of multiple large samples. Neuropsychopharmacology 48, 281–289.
[70] Núnez, P., Poza, J., Gómez, C., Rodríguez-González, V., Hillebrand, A., Tola-Arribas, M.A., Cano, M., Hornero, R., 2019. Characterizing the fluctuations of dynamic resting-state electrophysiological functional connectivity: reduced neuronal coupling variability in mild cognitive impairment and dementia due to alzheimer's disease. Journal of neural engineering 16, 056030.
[71] Otero, M., Lea-Carnall, C., Prado, P., Escobar, M.J., El-Deredy, W., 2022. Modelling neural entrainment and its persistence: influence of frequency of stimulation and phase at the stimulus offset. Biomedical Physics & Engineering Express 8, 045014.
[72] Otero, M., Prado-Gutiérrez, P., Weinstein, A., Escobar, M.J., El-Deredy, W., 2020. Persistence of eeg alpha entrainment depends on stimulus phase at offset. Frontiers in human neuroscience 14, 139.
[73] Pauls, K.A.M., Korsun, O., Nenonen, J., Nurminen, J., Liljeström, M., Kujala, J., Pekkonen, E., Renvall, H., 2022. Cortical beta burst dynamics are altered in parkinson's disease but normalized by deep brain stimulation. NeuroImage 257, 119308.
[74] Polanía, R., Nitsche, M.A., Ruff, C.C., 2018. Studying and modifying brain function with non-invasive brain stimulation. Nature neuroscience 21, 174–187.
[75] Prado, P., Moguilner, S., Mejía, J.A., Sainz-Ballesteros, A., Otero, M., Birba, A., Santamaria-Garcia, H., Legaz, A., Fittipaldi, S., Cruzat, J., et al., 2023. Source space connectomics of neurodegeneration: one-metric approach does not fit all. Neurobiology of disease 179, 106047.
[76] Rabinovich, M.I., Huerta, R., Varona, P., Afraimovich, V.S., 2008. Transient cognitive dynamics, metastability, and decision making. PLoS computational biology 4, e1000072.
[77] Rowland, N.C., De Hemptinne, C., Swann, N.C., Qasim, S., Miocinovic, S., Ostrem, J.L., Knight, R.T., Starr, P.A., 2015. Task-related activity in sensorimotor cortex in parkinson's disease and essential tremor: changes in beta and gamma bands. Frontiers in human neuroscience 9, 512.
[78] Sabidussi, G., 1966. The centrality index of a graph. Psychometrika 31, 581–603.
[79] Schnitzler, A., Gross, J., 2005. Normal and pathological oscillatory communication in the brain. Nature reviews neuroscience 6, 285–296.
[80] Schoonhoven, D.N., Briels, C.T., Hillebrand, A., Scheltens, P., Stam, C.J., Gouw, A.A., 2022. Sensitive and reproducible meg resting-state metrics of functional connectivity in alzheimer's disease. Alzheimer's Research & Therapy 14, 38.
[81] Schutter, D.J., Knyazev, G.G., 2012. Cross-frequency coupling of brain oscillations in studying motivation and emotion. Motivation and emotion 36, 46–54.
[82] Sharbafshaaer, M., Cirillo, G., Esposito, F., Tedeschi, G., Trojsi, F., 2024. Harnessing brain plasticity: The therapeutic power of repetitive transcranial magnetic stimulation (rtms) and theta burst stimulation (tbs) in neurotransmitter modulation, receptor dynamics, and neuroimaging for neurological innovations. Biomedicines 12, 2506.
[83] Snyder, A.Z., 1992. Steady-state vibration evoked potentials: description of technique and characterization of responses. Electroencephalography and Clinical Neurophysiology/Evoked Potentials Section 84, 257–268. doi:https://doi.org/10.1016/0168-5597(92)90007-X.
[84] Solomon, E.A., Sperling, M.R., Sharan, A.D., Wanda, P.A., Levy, D.F., Lyalenko, A., Pedisich, I., Rizzuto, D.S., Kahana, M.J., 2021. Theta-burst stimulation entrains frequency-specific oscillatory responses. Brain stimulation 14, 1271–1284.
[85] Spaak, E., de Lange, F.P., Jensen, O., 2014. Local entrainment of alpha oscillations by visual stimuli causes cyclic modulation of perception. Journal of Neuroscience 34, 3536–3544. doi:10.1523/JNEUROSCI.4385-13.2014.
[86] Storch, S., Samantzis, M., Balbi, M., 2021. Driving oscillatory dynamics: neuromodulation for recovery after stroke. Frontiers in Systems Neuroscience 15, 712664.
[87] Sun, L., Liang, X., Duan, D., Liu, J., Chen, Y., Wang, X., Liao, X., Xia, M., Zhao, T., He, Y., 2022. Structural insight into the individual variability architecture of the functional brain connectome. NeuroImage 259, 119387.
[88] Tanaka-Koshiyama, K., Koshiyama, D., Miyakoshi, M., Joshi, Y.B., Molina, J.L., Sprock, J., Braff, D.L., Light, G.A., 2020. Abnormal spontaneous gamma power is associated with verbal learning and memory dysfunction in schizophrenia. Frontiers in Psychiatry 11, 832.
[89] Terence W. Picton, M. Sasha John, A.D., Purcell, D., 2003. Human auditory steady-state responses: Respuestas auditivas de estado estable en humanos. International Journal of Audiology 42, 177–219. doi:10.3109/14992020309101316.
[90] Torres, F.A., Otero, M., Lea-Carnall, C.A., Cabral, J., Weinstein, A., El-Deredy, W., 2024. Emergence of multiple spontaneous coherent subnetworks from a single configuration of human connectome coupled oscillators model. Scientific Reports 14, 30726.
[91] Tzourio-Mazoyer, N., Landeau, B., Papathanassiou, D., Crivello, F., Etard, O., Delcroix, N., Mazoyer, B., Joliot, M., 2002. Automated anatomical labeling of activations in spm using a macroscopic anatomical parcellation of the mni mri single-subject brain. Neuroimage 15,

273–289.

[92] Von Stein, A., Sarnthein, J., 2000. Different frequencies for different scales of cortical integration: from local gamma to long range alpha/theta synchronization. International journal of psychophysiology 38, 301–313.

[93] Williams, L.M., 2016. Precision psychiatry: a neural circuit taxonomy for depression and anxiety. The Lancet Psychiatry 3, 472–480.

[94] Wilson, H.R., Cowan, J.D., 1972. Excitatory and inhibitory interactions in localized populations of model neurons. Biophysical journal 12, 1–24.

[95] Wolff, A., Berberian, N., Golesorkhi, M., Gomez-Pilar, J., Zilio, F., Northoff, G., 2022. Intrinsic neural timescales: temporal integration and segregation. Trends in cognitive sciences 26, 159–173.

[96] Ye, X., Li, L., He, R., Jia, Y., Poon, W., 2022. Rhythmic auditory stimulation promotes gait recovery in parkinson's patients: A systematic review and meta-analysis. Frontiers in Neurology 13, 940419.

[97] Zhang, W., Li, C., Wang, X., Liu, S., Ming, D., 2023. Boosting working memory performance by cross-frequency transcranial alternating current stimulation over the fronto-parietal network at theta and gamma frequency. Brain Stimulation: Basic, Translational, and Clinical Research in Neuromodulation 16, 301.

[98] Zhou, J., Greicius, M.D., Gennatas, E.D., Growdon, M.E., Jang, J.Y., Rabinovici, G.D., Kramer, J.H., Weiner, M., Miller, B.L., Seeley, W.W., 2010. Divergent network connectivity changes in behavioural variant frontotemporal dementia and alzheimer's disease. Brain 133, 1352–1367.

8. Supplementary Material

8.1. Forced Kuramoto Model Parameter

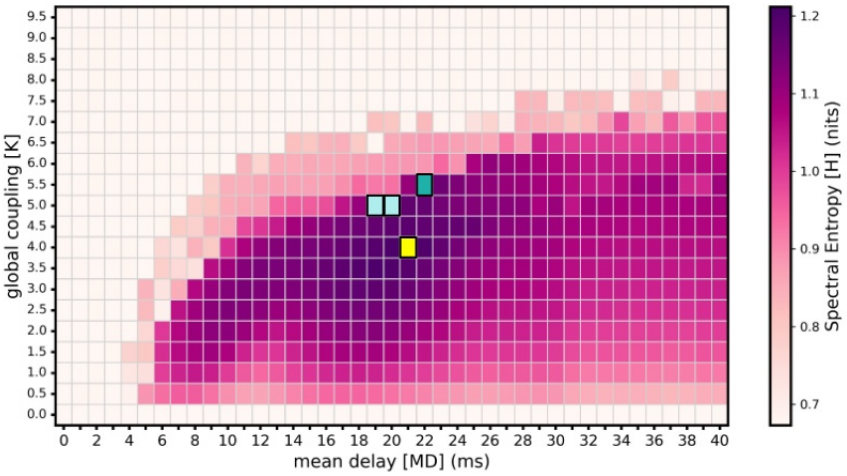

Figure S1: Spectral entropy in the parameter space exploration of global coupling (K) and mean delay (MD). The yellow square highlights the maximun value of spectral entropy. The blue squares represents de location of the fitting real EEG data.

8.2. Metastable oscillatory modes

To better understand the temporal dynamics of metastable brain states, we analyzed the metastable oscillatory modes (MOMs) durations across different values of K and MD. MOMs duration reflects the stability of transient oscillatory states, providing insights into how long specific frequency components remain dominant before the system transitions to another state [15]. Investigating these durations helps characterize the balance between stability and flexibility in the network's activity under different parameter settings.

MOM duration was defined as the time during which power remained above a threshold [15]. To determine this threshold for each combination of K and MD, z-scores were computed from the Hilbert envelopes across all nodes and frequency bands, applying a threshold of 2 for MOMs detection [19].

To examine the spatial distribution of dominant oscillatory activity, we generated brain plots for each pair of K and MD. In these plots, nodes were color-coded according to the frequency band in which their peak activity occurred (delta, theta, alpha, beta, or gamma). As shown in Figure S2, for simulations performed with K and MD values selected due to their close match with EEG spectral features, the alpha band emerged as the predominant component, both in terms of duration and spatial distribution. However, this predominance was not observed across the entire parameter space, indicating that the selected values of K and MD are particularly relevant for replicating EEG-like oscillatory behavior.

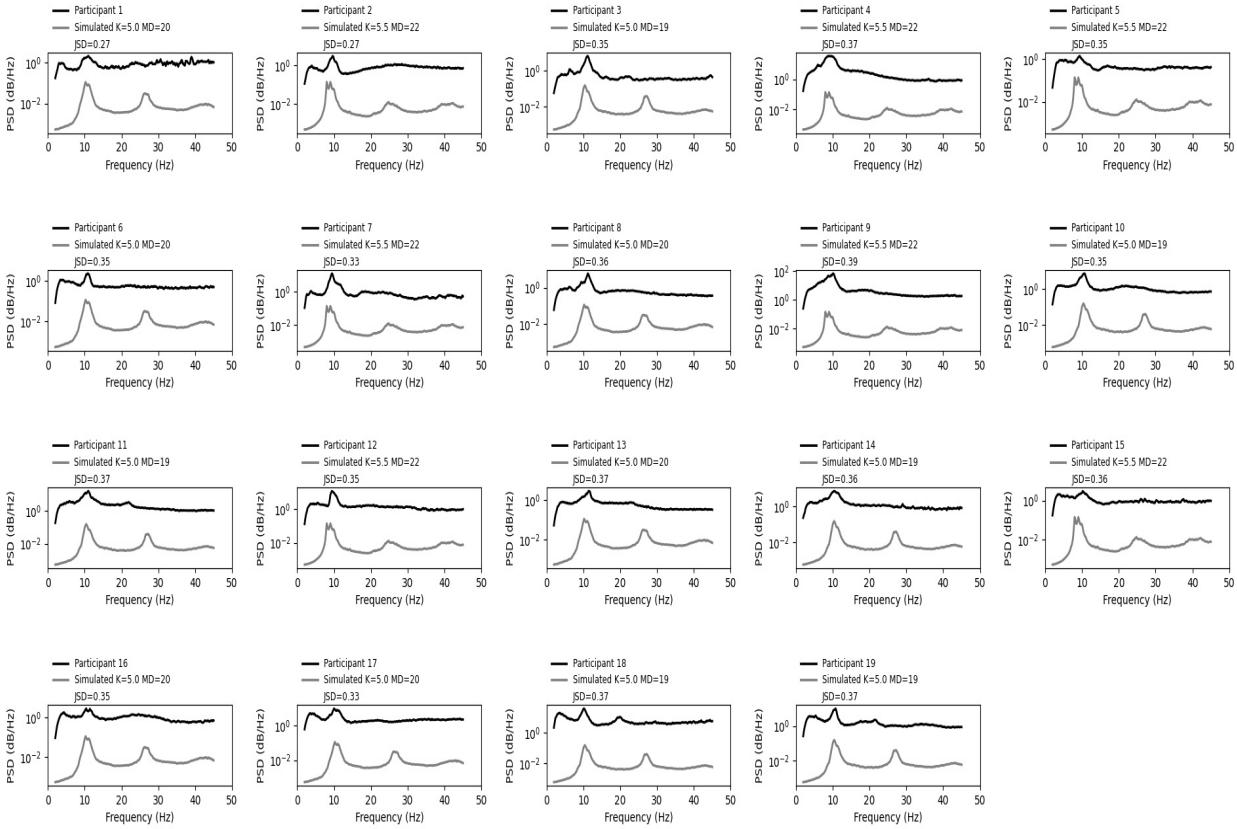

Figure S2: Mapping the spectrum from the kuramoto model to the spectrum of real EEG subjects. It shows the spectrum of the Kuramoto model (marked in gray) that had the smallest Jensen-Shannon (JS) distance compared to the real EEG spectra of the subjects (marked in black).

8.3. Structural Metrics of a Network

To find the structural metric of the network that showed the highest linear correlation with the number of entrained nodes, a study was carried out on the following features:

Weight: It represents the strength or capacity of the connection. It is calculated as:

$$w_n = \sum_{p=1}^{N} w_{np} \tag{9}$$

Where w_{np} represents the weight between n and p.

Betweenness centrality: It measures the extent to which a node lies on the shortest paths between other nodes [33].

$$C_B(v) = \sum_{n \neq v \neq p} \frac{\sigma_{np}(v)}{\sigma_{np}} \tag{10}$$

Where σ_{np} is the total number of shortest paths between nodes n and p, and $\sigma_{np}(v)$ is the number of those paths that pass through node v.

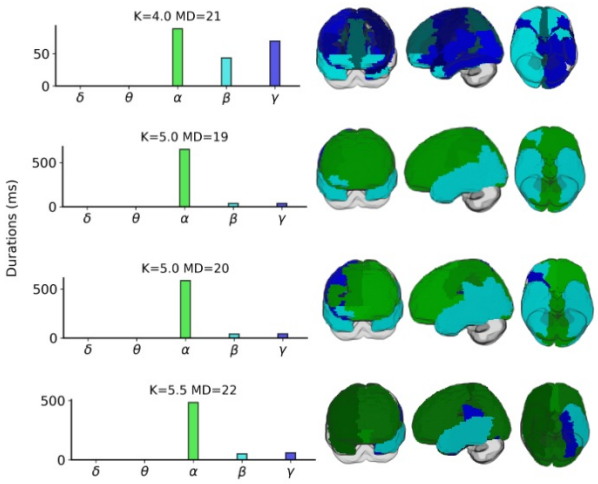

Figure S3: The figure shows the MOMs duration of each band for each K and MD combinations. The second column shows the spatial distribution of preferred frequencies per K and MD combinations. Each frequency band is represented by a color gradient to indicate lower or higher frequencies. δ: 0.5-4 Hz, θ: 4-8 Hz, α: 8-13 Hz, β: 13-30 Hz, γ: 30-45 Hz.

Degree centrality: It measures the number of direct connections a node has.

$$k_n = \sum_p a_{np} \tag{11}$$

Where a_{np} is 1 if there is an edge between n and p, and 0 otherwise.

Closeness centrality: It measures how quickly a node can reach other nodes in the network. It is based on the inverse of the average shortest path length from a node to all other nodes in the network [78].

$$C_C(n) = \frac{N-1}{\sum_p d(n,p)} \tag{12}$$

Where $d(n,p)$ is the shortest path distance between nodes n and p, and N is the total number of nodes.

8.4. Neural Entrainment

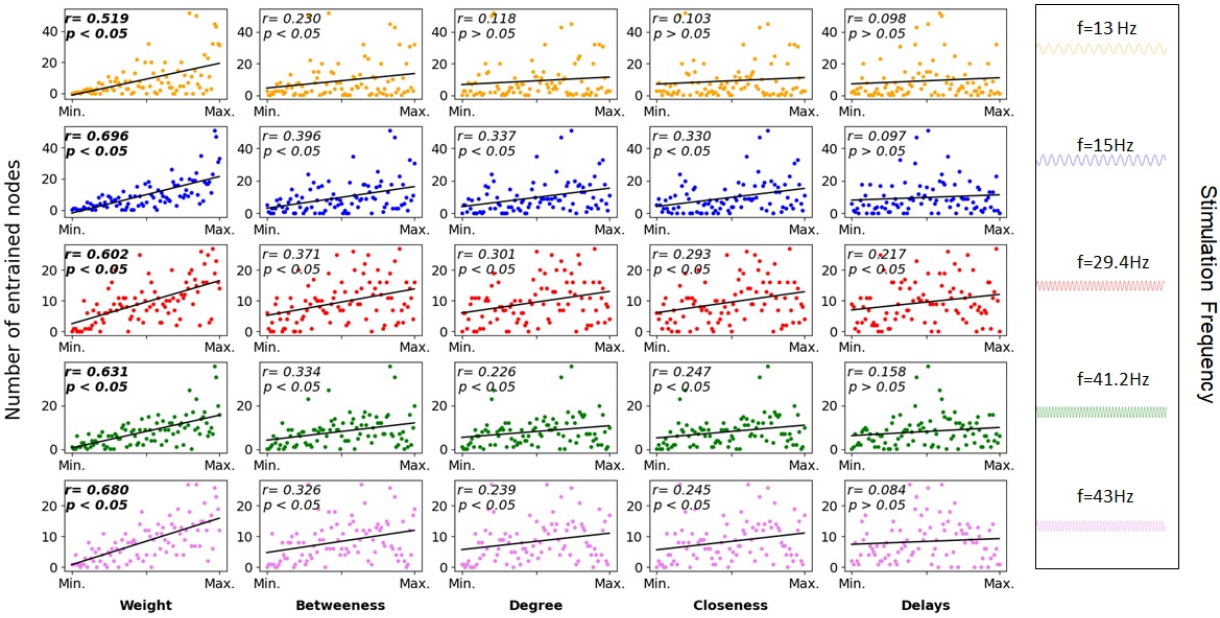

Figure S4: Stimulation effects across nodes at different frequencies, sorted by structural features (Weighted Degree, Degree, Closeness, Betweenness, Delays). Each column displays nodes in descending order based on the corresponding feature, along with a linear fit. Across all frequencies, node weighted degree showed the strongest linear association with stimulation effects.

Label	Region short name	Region name	Label	Region short name	Region name
1	L Precentral	Precentral gyrus Left	46	R Cuneus	Cuneus Right
2	R Precentral	Precentral gyrus Right	47	L Lingual	Lingual gyrus Left
3	L Frontal Sup	Superior frontal gyrus (dorsolateral) Left	48	R Lingual	Lingual gyrus Right
4	R Frontal Sup	Superior frontal gyrus (dorsolateral) Right	49	L Occipital Sup	Superior occipital gyrus Left
5	L Front Sup Orb	Middle frontal gyrus (orbital part) Left	50	R Occipital Sup	Superior occipital gyrus Right
6	R Front Sup Orb	Middle frontal gyrus (orbital part) Right	51	L Occipital Mid	Middle occipital gyrus Left
7	L Front Mid	Middle frontal gyrus Left	52	R Occipital Mid	Middle occipital gyrus Right
8	R Front Mid	Middle frontal gyrus Right	53	L Occipital Inf	Inferior occipital gyrus Left
9	L Front Mid Orb	Middle frontal gyrus (orbital part) Left	54	R Occipital Inf	Inferior occipital gyrus Right
10	R Front Mid Orb	Middle frontal gyrus (orbital part) Right	55	L Fusiform	Fusiform gyrus Left
11	L Front Inf Ope	Inferior frontal gyrus (opercular part) Left	56	R Fusiform	Fusiform gyrus Right
12	R Front Inf Ope	Inferior frontal gyrus (opercular part) Right	57	L Postcentral	Postcentral gyrus Left
13	L Front Inf Tri	Inferior frontal gyrus (triangular part) Left	58	R Postcentral	Postcentral gyrus Left
14	R Front Inf Tri	Inferior frontal gyrus (triangular part) Right	59	L Parietal Sup	Superior parietal gyrus Left
15	L Front Inf Orb	Inferior frontal gyrus (orbital part) Left	60	R Parietal Sup	Superior parietal gyrus Right
16	R Front Inf Orb	Inferior frontal gyrus (orbital part) Right	61	L Parietal Inf	Inferior parietal but supramarginal and angular gyri Left
17	L Rolandic Oper	Rolandic operculum Left	62	R Parietal Inf	Inferior parietal but supramarginal and angular gyri Right
18	R Rolandic Oper	Rolandic operculum Right	63	L SupraMarginal	Supramarginal gyrus Left
19	L Supp Motor Ar	Supplementary motor area Left	64	R SupraMarginal	Supramarginal gyrus Right
20	R Supp Motor Ar	Supplementary motor area Right	65	Left Angular	Angular gyrus Left
21	L Olfactory	Olfactory cortex Left	66	R Angular	Angular gyrus Right
22	R Olfactory	Olfactory cortex Right	67	L Precuneus	Precuneus Left
23	L Front Sup Med	Superior frontal gyrus (medial) Left	68	R Precuneus	Precuneus Right
24	R Front Sup Med	Superior frontal gyrus (medial) Right	69	L Paracentr Lob	Paracentral lobule Left
25	L Front Med Orb	Superior frontal gyrus (medial orbital) Left	70	R Paracentr Lob	Paracentral lobule Right
26	R Front Med Orb	Superior frontal gyrus (medial orbital) Right	71	L Caudate	Caudate nucleus Left
27	L Rectus	Rectus gyrus Left	72	R Caudate	Caudate nucleus Right
28	R Rectus	Rectus gyrus Right	73	L Putamen	Lenticular nucleus putamen Left
29	L Insula	Insula Left	74	R Putamen	Lenticular nucleus putamen Right
30	R Insula	Insula Right	75	L Pallidum	Lenticular nucleus pallidum Left
31	L Cingulum Ant	Anterior cingulate and paracingulate gyri Left	76	R Pallidum	Lenticular nucleus pallidum Right
32	R Cingulum Ant	Anterior cingulate and paracingulate gyri Right	77	L Thalamus	Thalamus Left
33	L Cingulum Mid	Median cingulate and paracingulate gyri Left	78	R Thalamus	Thalamus Right
34	R Cingulum Mid	Median cingulate and paracingulate gyri Right	79	L Heschl	Heschl gyrus Left
35	L Cingulum Post	Posterior cingulate gyrus Left	80	R Heschl	Heschl gyrus Right
36	R Cingulum Post	Posterior cingulate gyrus Right	81	L Temporal Sup	Superior temporal gyrus Left
37	Left Hippocampus	Hippocampus Left	82	R Temporal Sup	Superior temporal gyrus Right
38	R Hippocampus	Hippocampus Right	83	L Tempr Pol Sup	Temporal pole: superior temporal gyrus Left
39	L ParaHippocamp	Parahippocampal gyrus Left	84	R Tempr Pol Sup	Temporal pole: superior temporal gyrus Right
40	R ParaHippocamp	Parahippocampal gyrus Right	85	L Temporal Mid	Middle temporal gyrus Left
41	L Amygdala	Amygdala Left	86	R Temporal Mid	Middle temporal gyrus Right
42	R Amygdala	Amygdala Right	87	L Tempr Pol Mid	Temporal pole: middle temporal gyrus Left
43	L Calcarine	Calcarine fissure and surrounding cortex Left	88	R Tempr Pol Mid	Temporal pole: middle temporal gyrus Right
44	R Calcarine	Calcarine fissure and surrounding cortex Right	89	L Temporal Inf	Inferior temporal gyrus Left
45	L Cuneus	Cuneus Left	90	R Temporal Inf	Inferior temporal gyrus Right

Table S1
Glossary of AAL90 regions

Frequency (Hz)	13				29,4				43			
Parameters combinations	K=4 MD=21	K=5 MD=19	K=5 MD=20	K=5.5 MD=22	K=4 MD=21	K=5 MD=19	K=5 MD=20	K=5.5 MD=22	K=4 MD=21	K=5 MD=19	K=5 MD=20	K=5.5 MD=22
Nodes increasing SE	45	31	48	34	35	20	27	37	29	19	17	23
Nodes decreasing SE	45	59	42	56	55	70	63	53	61	71	73	67
Δ SE	-0.038	-0.013	0.004	-0,016	-0.011	-0.022	-0.011	-0,047	-0.013	-0.031	-0.018	-0,212

Table S2
Changes in spectral entropy relative to the pre-stimulation baseline for 13 Hz, 29.4 Hz, and 43 Hz stimulation of the right precuneus across different $\{K, MD\}$ parameter combinations. The table reports the number of nodes showing increased or decreased spectral entropy (SE), along with the total change in SE (Δ SE) for each condition. At higher stimulation frequencies, reductions in SE were more prevalent, leading to consistently negative Δ SE values across all tested configurations.

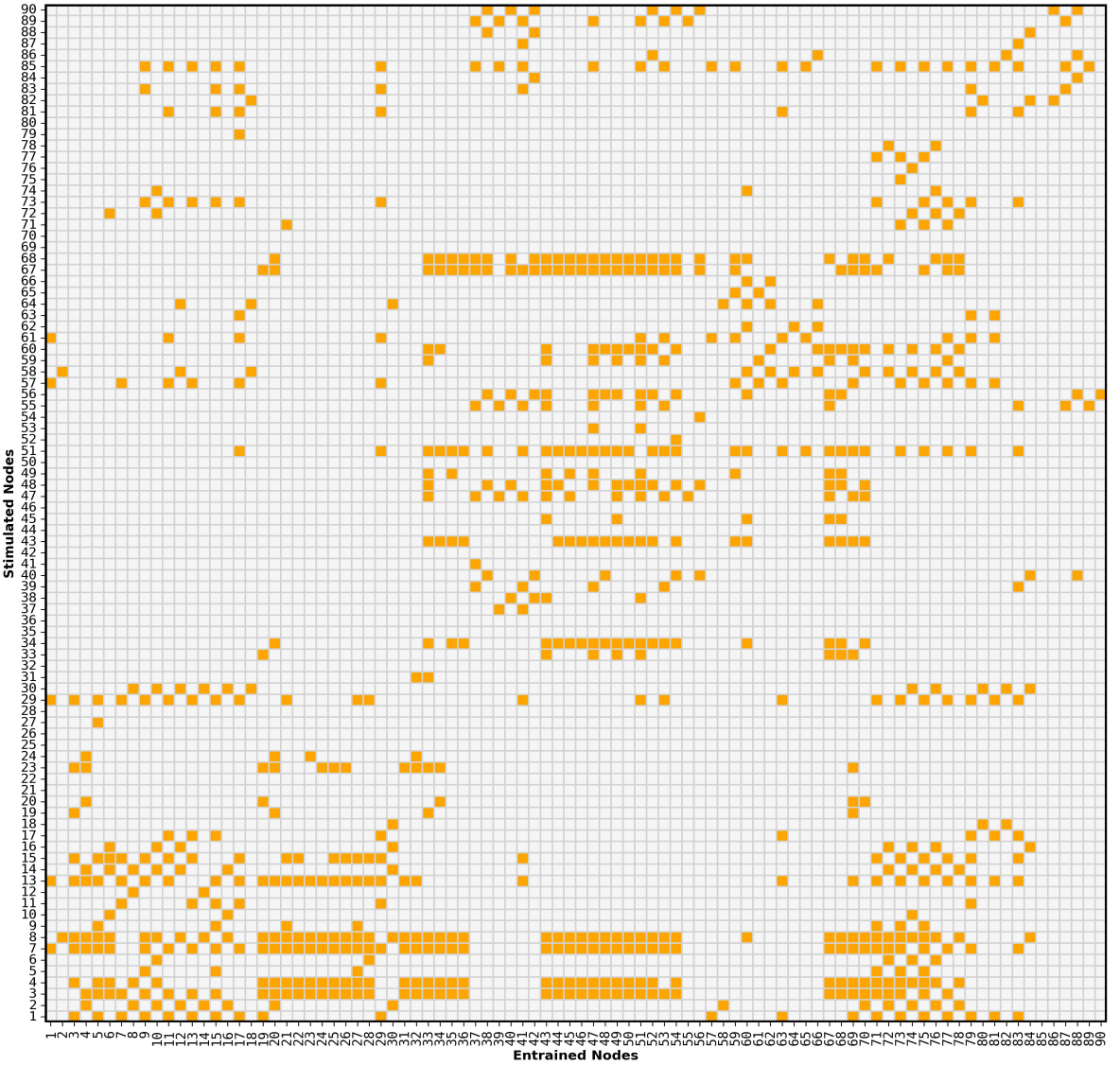

Figure S5: Entrainment of the nodes by stimulating each node of the network at the point of maximum entropy (K=4, MD=21) and for a frequency of 13 Hz. To check the correspondence between the numbers and the AAL90 regions see Tab. S1

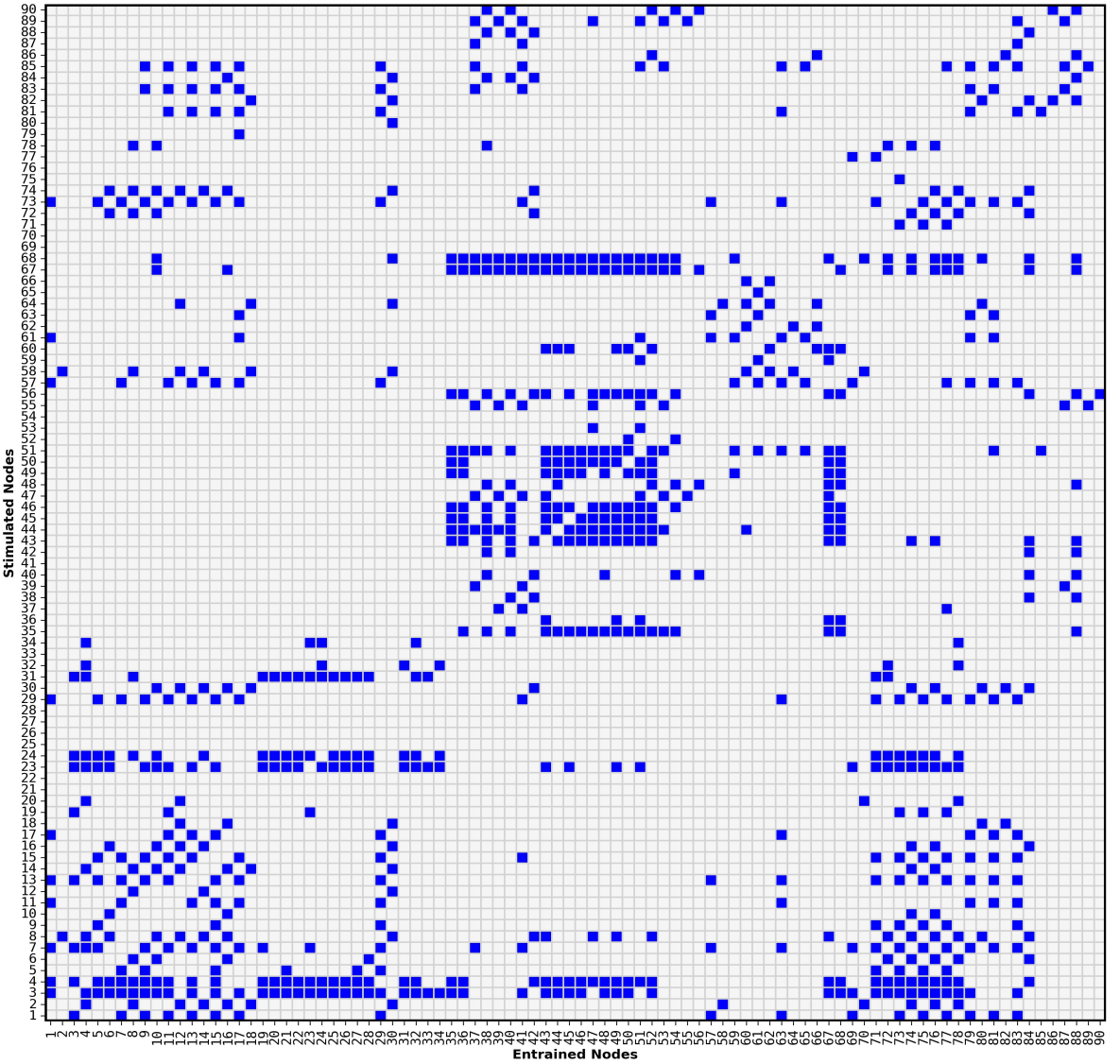

Figure S6: Entrainment of the nodes by stimulating each node of the network at the point of maximum entropy (K=4, MD=21) and for a frequency of 15 Hz. To check the correspondence between the numbers and the AAL90 regions see Tab. S1

Figure S7: Entrainment of the nodes by stimulating each node of the network at the point of maximum entropy (K=4, MD=21) and for a frequency of 29.4 Hz. To check the correspondence between the numbers and the AAL90 regions see Tab. S1

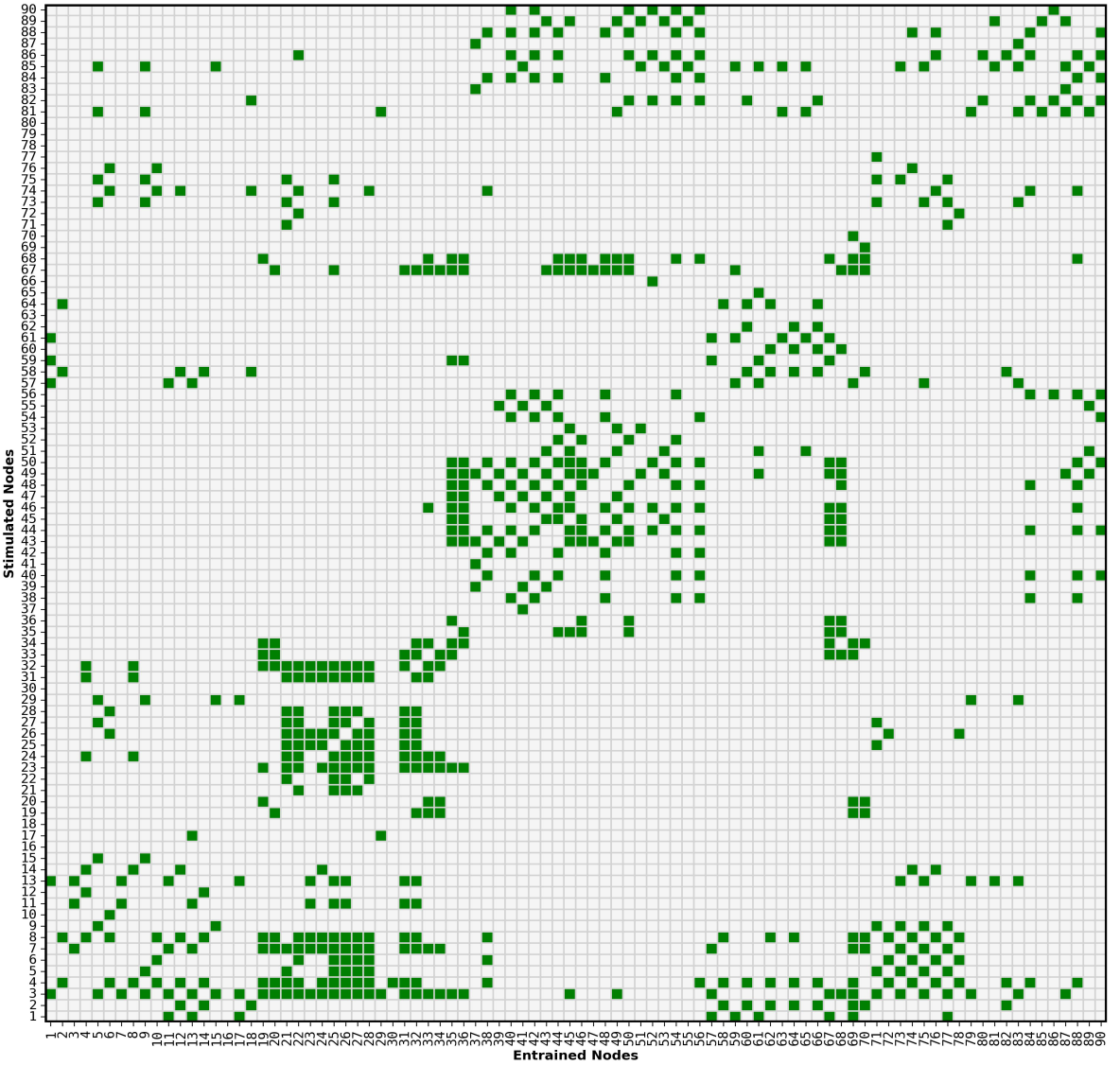

Figure S8: Entrainment of the nodes by stimulating each node of the network at the point of maximum entropy (K=4, MD=21) and for a frequency of 41.2 Hz. To check the correspondence between the numbers and the AAL90 regions see Tab. S1

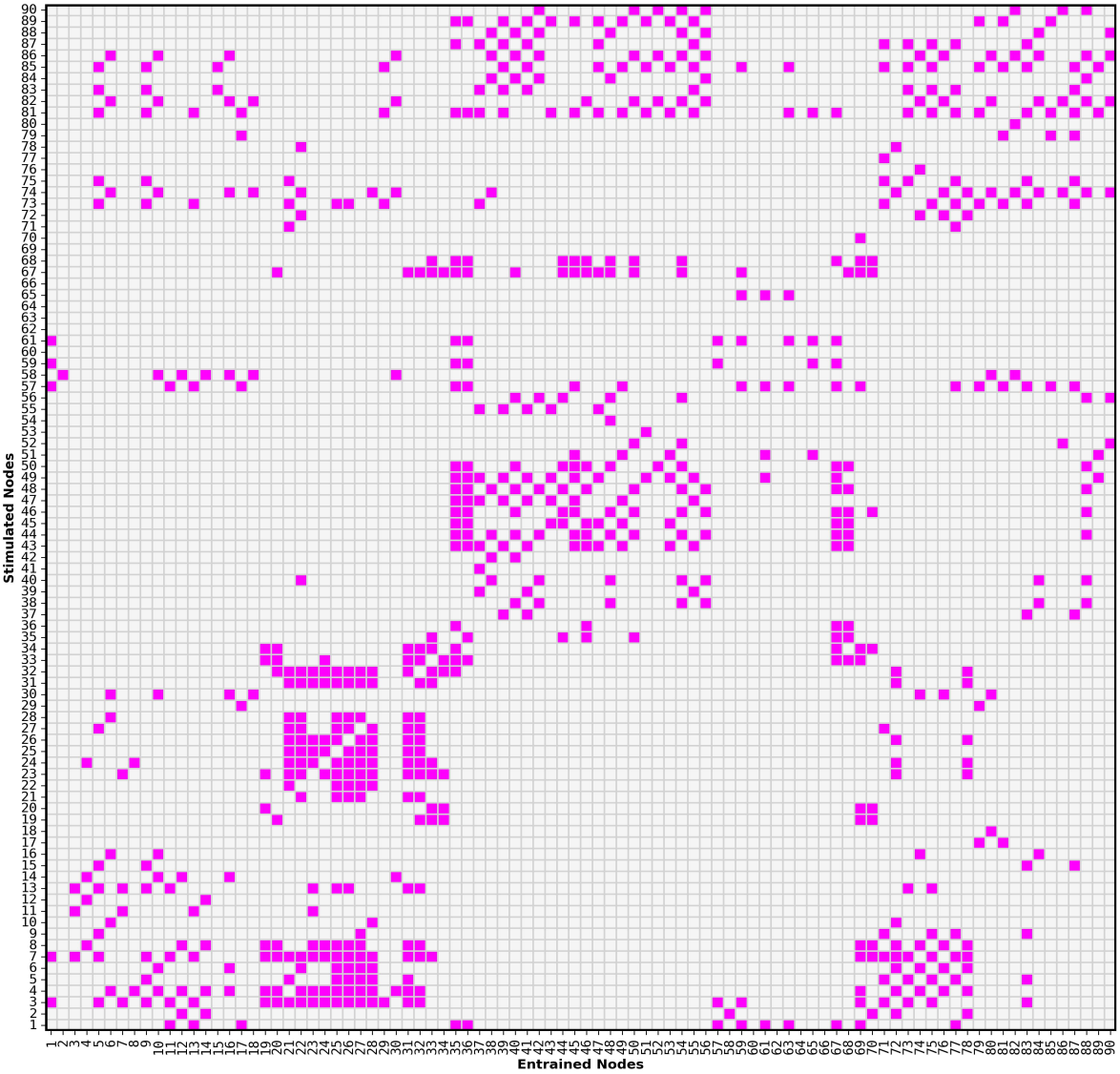

Figure S9: Entrainment of the nodes by stimulating each node of the network at the point of maximum entropy (K=4, MD=21) and for a frequency of 43 Hz. To check the correspondence between the numbers and the AAL90 regions see Tab. S1

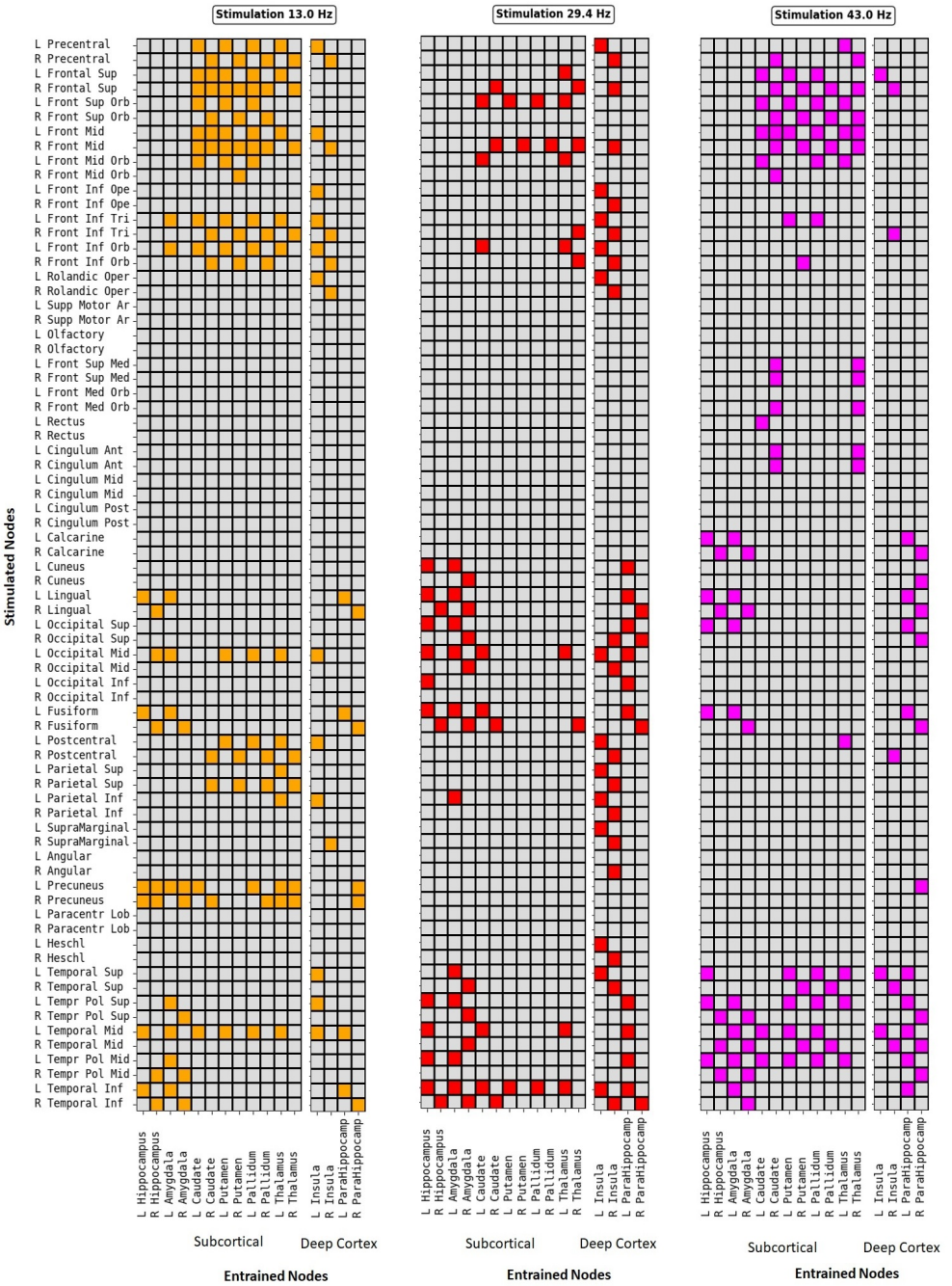

Figure S10: Nodes on Y-axis are stimulated at 13Hz (A), 29.4Hz (B), or 43Hz (C) at maximum metastability K,MD=4, 21ms. Nodes on the X-axis are subcortical and deep cortical structures entrained to the driving frequency although they are not directly connected to the stimulated nodes. As in Figure 3, 13Hz reaches a widespread network, whereas 43Hz led to localized effects, with minimal propagation beyond the cortical stimulation site

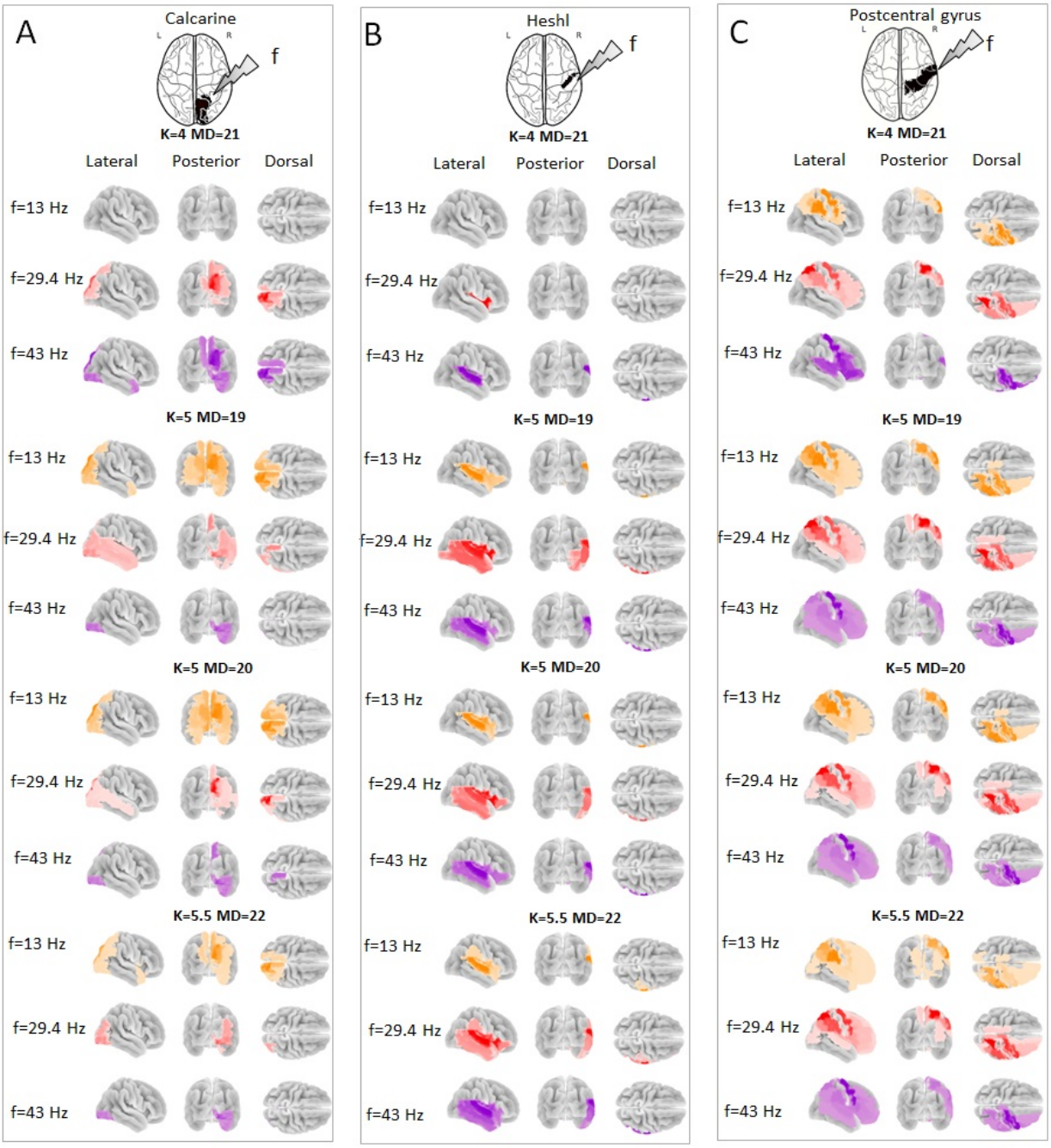

Figure S11: Effect of stimulation across combinations of K and MD values, analyzed at different stimulation frequencies. The primary nodes stimulated belong to the right hemisphere of the visual cortex (A: Calcarine), auditory cortex (B: Heschl), and somatosensory cortex (C: Postcentral gyrus).